Research Square

Preprints are preliminary reports that have not undergone peer review.
They should not be considered conclusive, used to inform clinical practice,
or referenced by the media as validated information.

From Radial Oscillatory Functions to Nonlinear Dynamical Systems with Damping: A Complete Construction with Feedback, Bifurcation, and Chaos

Hasan Akin

akinhasan@harran.edu.tr

Harran University

Research Article

Keywords: Nonlinear dynamics, pulsating attractor, symmetry breaking, chaos, strange attractor, stochastic dynamics, radial oscillations

Posted Date: May 27th, 2026

DOI: https://doi.org/10.21203/rs.3.rs-9738166/v1

License: This work is licensed under a Creative Commons Attribution 4.0 International License.
Read Full License

Additional Declarations: No competing interests reported.

From Radial Oscillatory Functions to Nonlinear Dynamical Systems with Damping: A Complete Construction with Feedback, Bifurcation, and Chaos

Hasan Akın[a,]

[a]*Department of Mathematics, Faculty of Arts and Sciences, Harran University, TR63050, Sanliurfa, Turkey*

Abstract

In this study, we propose a formal construction and multifaceted analysis of a novel two-dimensional nonlinear dynamical system derived from radially symmetric oscillatory functions with transcendental exponential damping characteristics. Numerical simulations and theoretical analyses reveal that the $(1 - r^2)$ feedback mechanism, coupled with intrinsic phase-dependent terms, induces a stable pulsating attractor that oscillates within a narrow annular region around the unit manifold. This structural property persists across a wide range of damping parameters and serves as a robust framework for complex dynamics. To investigate the transition to high-dimensional complexity, we introduce a non-autonomous periodic forcing term, which triggers a route to chaos characterized by a strange attractor with a distinct fractal topology. Furthermore, we extend the deterministic model into a stochastic framework using Itô-type Stochastic Differential Equations (SDEs) to assess its robustness under biological-like noise. Numerical integrations using the Euler-Maruyama scheme revealed that the system maintained a "stochastic pulsating attractor," where the trajectories remained confined within a stable boundary despite continuous perturbations. These results suggest that the proposed model provides a versatile and robust mathematical framework for simulating complex neuronal oscillations and signal propagation in dissipative, nonlinear media.

Keywords: Nonlinear dynamics, pulsating attractor, symmetry breaking, chaos, strange attractor, stochastic dynamics, radial oscillations.

Contents

1 Introduction **2**

2 Theoretical Framework and Model Construction **5**

2.1 Continuous-Time Vector Field 5
2.2 A Formal One-Dimensional Reduction 5
2.3 Associated Discrete Iteration 5
2.4 Geometric Interpretation of the Vector Field 6
2.5 Dimensional Reduction and Symmetry Analysis 6
2.6 Characterization of Transcendental Components 7
2.7 Topological Invariants: The Rotation Number 7
2.8 Dual Recurrence Systems and Iterative Evolution 7
2.8.1 Convergence and Orbital Divergence 7
2.9 Lyapunov Spectra, Rotation-Like Quantities, and Bifurcation Structures under a π-Scaled Modification 8

Email address: akinhasan@harran.edu.tr; akinhasan25@gmail.com (Hasan Akın)

3 Full Oscillatory Damping Feedback Dynamics **10**
3.1 Boundedness and the Poincaré–Bendixson Framework . . . 10
3.2 Numerical Verification of Orbital Stability . . . 12
3.3 Numerical Results and Dynamical Verification . . . 13
3.4 Stability and Bifurcation Analysis . . . 13
3.5 Structural Dynamics of the Unforced System . . . 14
3.6 Full Oscillatory Feedback and Chaos . . . 14
3.7 Physical Interpretation of the Oscillatory Feedback Loop . . . 15

4 Forced Oscillatory Feedback and Nonlinear Dynamics **16**
4.1 Numerical Results and Chaos Analysis . . . 19
4.2 Non-autonomous Forcing and the Emergence of Complex Dynamics . . . 20
4.3 Characterization of Deterministic Chaos: Bifurcation and Lyapunov Analysis . . . 21
4.4 Stroboscopic Sampling and Morphological Analysis . . . 22
4.5 Theoretical Context and Comparative Analysis of Phase Portraits and Poincaré Sections . . . 24

5 Stochastic Extension of the Oscillatory Damping Feedback Systems **29**
5.1 Stochastic Dynamics of the Autonomous Oscillatory Damping Feedback Regime . . . 29
5.2 Stochastic Transitions in Forced Regime . . . 31
5.2.1 Numerical Integration: Euler–Maruyama Scheme . . . 32
5.2.2 Attractor Dynamics and Stochastic Stability . . . 32
5.2.3 Numerical Results and Attractor Analysis under Stochastic Forcing . . . 32
5.3 Numerical Results and Dynamical Analysis . . . 35
5.4 Power Spectral Density Analysis . . . 36

6 Conclusions **36**

Appendix A Polar Representation of the Dynamical System **40**
Appendix A.1 Polar Coordinate Transformation . . . 40
Appendix A.2 Unforced System ($A = B = 0$) . . . 40
Appendix A.3 Forcing Contribution . . . 41
Appendix A.4 Full Polar System . . . 41
Appendix A.5 Auxiliary Variable . . . 41
Appendix A.6 Structural Remark . . . 41

1. Introduction

In [1], the authors investigate the active suppression of oscillations in lightly damped linear systems subject to uncertain or time-varying parameters. Their approach is applicable to systems possessing an arbitrary number of vibrational modes. In [2], Yang and Feng introduced a gain-tunable cross-coupled n-dimensional sinusoidal discrete hyperchaotic system and presented a dual-chaotic image encryption scheme via dynamic parameter modulation, as well as an FPGA CORDIC-based implementation of a 3D chaotic core that confirmed fixed-point feasibility and numerical consistency. While the Lyapunov spectrum quantitatively measures chaos (positive Lyapunov exponent = chaos), the bifurcation diagram provides a qualitative representation. Together, they allow for a complete understanding of the dynamic behavior of the system [3, 4, 5]. In [6], an exponential chaotic oscillator was proposed by adding an exponential nonlinear term to the classical Lü system. The study includes dynamic analyses such as phase diagrams, equilibrium point stability, Poincaré mappings, Lyapunov exponent spectra and bifurcation diagrams.

One of the most fundamental tools for characterizing nonlinear dynamical systems is the Lyapunov exponent, which quantifies the exponential divergence or convergence of nearby trajectories in the phase space [7]. A positive maximal Lyapunov exponent serves as the hallmark of deterministic indicating a sensitive dependence on the initial conditions [8]. Beyond merely detecting chaos, the Lyapunov exponent provides crucial insights into the stability of periodic orbits, bifurcations, and the transition to turbulence [3]. Moreover, the Lyapunov spectrum is intimately connected to the fractal dimension of strange attractors through the Kaplan–Yorke conjecture [9, 10]. In applied contexts, Lyapunov exponents have been used to analyze birhythmicity in biological oscillators [11], to characterize chaotic dynamics in electronic circuits [6], and to design chaotic systems for encryption applications [2]. The reliable numerical computation of Lyapunov exponents, particularly for high-dimensional or stochastic systems, remains an active area of research [12, 13, 14].

Several studies have investigated the nonlinear dynamics of biological oscillators. In [11], Enjieu Kadji et al. analyzed a biological system modeled using a multi-limit cycle Van der Pol oscillator. Using analytical and numerical methods, the autonomous case reveals birhythmicity, whereas the non-autonomous case treats harmonic oscillations and their stability limits. Foundational results on turbulence and strange attractors were established by Ruelle and Takens [15] and Newhouse, Ruelle, and Takens [16]. Uezu and Davis [17] investigated the scaling of Lyapunov exponents and the widths of resonance horns (Arnold tongues) in both subcritical and supercritical regions of the sine circle map, providing fundamental insights into the transition to chaos in forced oscillatory systems. Subsequently, Davie [18] provided a comprehensive analysis of the width of Arnold tongues.

Radial oscillatory functions with damping arise naturally in various physical and engineering contexts, such as wave propagation in dissipative media. When embedded into dynamical systems, these functions can generate rich and nonlinear behaviors. In this work, we develop a systematic construction starting from a basic scalar oscillatory profile and leading to a complex nonlinear dynamical system incorporating feedback mechanisms and chaotic forcing. We show that our system exhibits a distinctive structure that differentiates it from classical nonlinear oscillators, such as the Hopf, van der Pol, and Stuart–Landau models [8, 19, 20]. Specifically, the drift terms integrate a nonlinear radial feedback with **transcendental functions** of r^2, further modulated by an **amplitude-dependent exponential damping factor**.

While individual components of this formulation, such as saturation terms or damping effects, are well established in the theory of nonlinear oscillations [8, 21], their specific integration in the form of (12) represents a significant departure from standard models. This architecture induces a **nontrivial coupling** between the amplitude and phase dynamics, yielding a rich spectrum of behaviors that are not captured by classical polynomial normal forms.

To the best of our knowledge, a systematic dynamical analysis of such a **transcendental, radially modulated oscillator** with exponential damping has not been reported in the literature. Unlike the classical Stuart–Landau oscillator, where the dynamics are governed by polynomial nonlinearities [20, 22], the present model incorporates **non-polynomial interactions**, leading to fundamentally different phase–amplitude landscapes. The robustness of these interactions is further explored through phase-locking analysis, where the emergence of stable synchronization regions, known as Arnold tongues, is documented under varying forcing parameters. Furthermore, we analyze the transition from periodic orbits to chaotic states, as evidenced by the bifurcation diagrams and spectral density analysis presented in the subsequent sections.

The chaotic properties of nonlinear dynamical systems in both one and higher dimensions have long been a fundamental area of research because of their capacity to explain complex physical and biological phenomena. In particular, systems built on transcendental functions tend to exhibit richer dynamical structures than standard polynomial models [23]. In this context, this study presents the formal construction and multifaceted analysis of a novel two-dimensional nonlinear dynamical system derived from radially symmetric oscillatory functions with exponential damping characteristics.

The dynamic structure of the proposed model is grounded in the unique stability properties emerging from the influence of the exponential terms utilized in the system design. It is recognized in the literature that oscillators containing exponential damping terms can produce asymmetric self-sustained oscillations and sudden jumps to instantaneous high values, often referred to as "excursions" [24]. In this study, we demonstrate through numerical simulations that the integration of the $(1 - r^2)$ feedback mechanism induces a stable limit cycle at $r = 1$. This periodic attractor persists across a wide range of damping parameters, providing a robust oscillatory baseline for the system.

To investigate the transition of the system from low-dimensional regular dynamics to high-dimensional complexity, a nonautonomous periodic forcing term was added to the model. This intervention triggers a route to chaos, characterized by a "strange attractor" with a distinct fractal topology. The detection of chaotic attractors is generally validated by at least one positive Lyapunov exponent and multilayered stratification in the Poincaré sections [25]. In this study, the chaotic nature of the system was quantitatively verified by calculating the positive maximal Lyapunov exponent and observing stratification in the Poincaré maps.

Furthermore, Arnold tongues, which represent frequency-locking regions in the parameter space, are critical for understanding the synchronization capabilities of such oscillator systems [26]. In particular, in systems with external forcing, the structure of Arnold tongues determines the boundaries of synchronization and the onset of chaos [27]. The deterministic model presented in our study was extended to a stochastic framework using Itô-type stochastic differential equations [28] to assess its robustness under biological-like noise. Numerical integrations using the Euler-Maruyama scheme revealed that the system maintained a "Stochastic Pulsating Attractor," where trajectories remained confined within a stable boundary despite continuous perturbations.

In this study, we develop a two-dimensional nonlinear dynamical system that incorporates damping, oscillatory behavior, and feedback interactions. The model is subsequently extended by introducing external forcing terms with varying amplitudes and frequencies, leading to a more general framework referred to as *forced oscillatory feedback and nonlinear dynamics*. Consequently, our findings suggest that the proposed model provides a versatile and robust mathematical framework for simulating complex processes such as neuronal oscillations and signal propagation in dissipative nonlinear media [29]. By combining theoretical dynamical analysis and stochastic modeling approaches, this study aims to contribute a unique architecture to the literature that deviates from conventional models.

The dynamical properties of the system are investigated using numerical methods based on the Itô calculus, with particular emphasis on the Lyapunov exponents and bifurcation diagrams. These indicators provide a systematic basis for identifying transitions between stable and chaotic regimes in both autonomous and externally driven settings. To further enhance the analysis, we extend the framework to a stochastic setting by constructing stochastic counterparts of both the unforced and forced systems. The Euler–Maruyama method is employed to examine deviations in system trajectories under random perturbations, allowing for a comprehensive assessment of the model's robustness in both deterministic and stochastic regimes.

The remainder of this paper is organized as follows. Section 2 establishes the theoretical framework and model construction, including the continuous-time vector field, dimensional reduction, topological invariants, and Lyapunov spectra. Section 3 analyzes the full autonomous oscillatory damping feedback dynamics, including boundedness, orbital stability, bifurcation analysis, and transition to chaos. Section 4 introduces external periodic forcing, leading to a nonautonomous system in which resonance phenomena (Arnold tongues), bifurcations, and chaotic dynamics are characterized using Lyapunov exponents, bifurcation diagrams, and stroboscopic sampling, respectively. Section 5 extends both the autonomous and forced regimes into a stochastic framework using Itô-type stochastic differential equations and the Euler–Maruyama scheme, examining the robustness of limit cycles and chaotic attractors under noise, and presenting power spectral density (PSD) analyses. Finally, Section 6 summarizes the main findings and

discusses potential applications. The polar representation of the dynamical system, including coordinate transformations and derivations for both the unforced and forced cases, is provided in the Appendix.

2. Theoretical Framework and Model Construction

In this section, we establish the theoretical framework and model construction, including the continuous-time vector field, dimensional reduction, topological invariants, and Lyapunov spectra.

2.1. Continuous-Time Vector Field

We consider the autonomous dynamical system in $\mathbb{R}^2$

$$\begin{cases} \dot{x} = \Phi(x,y) = \left[(1-r^2)\sin(r^2) - \cos(r^2)\right] e^{-ar^2}, \\ \dot{y} = \Psi(x,y) = \left[(1-r^2)\cos(r^2) + \sin(r^2)\right] e^{-ar^2}, \end{cases} \tag{1}$$

where $r^2 = x^2 + y^2$ and $a > 0$. The vector field is $\mathcal{C}^\infty$ smooth and involves non-polynomial nonlinearities through transcendental dependence on r^2.

2.2. A Formal One-Dimensional Reduction

To gain preliminary insight into the nonlinear structure of the model, we also consider a simplified one-dimensional reduction obtained by imposing a diagonal ansatz $y = x$. Under this restriction, the radial quantity becomes

$$r^2 = x^2 + y^2 = 2x^2.$$

Substituting this relation into the components of the vector field yields the reduced maps

$$\Phi_a(x) = \left[(1-2x^2)\sin(2x^2) - \cos(2x^2)\right] e^{-2ax^2}, \tag{2}$$

and

$$\Psi_a(x) = \left[(1-2x^2)\cos(2x^2) + \sin(2x^2)\right] e^{-2ax^2}. \tag{3}$$

We emphasize that this reduction is used as a simplified surrogate description and should not be interpreted as an invariant reduction of the full two-dimensional flow unless additional invariance conditions are verified in the future.

2.3. Associated Discrete Iteration

Motivated by the reduced expressions (5) and (6), we study the one-dimensional discrete-time iterations

$$x_{n+1} = \Phi_a(x_n), \qquad x_{n+1} = \Psi_a(x_n),$$

as auxiliary models to explore qualitative features such as asymptotic contraction, bifurcation structure, and parameter sensitivity. These discrete systems are not introduced as exact Poincaré maps of the continuous flow, but rather as reduced iterative analogs associated with the original vector field. In this section, we construct a reduced one-dimensional map from the original two-dimensional transcendental system to analyze its topological properties, as follows. The original system is governed by the functions $\phi(x,y)$ and $\psi(x,y)$, defined as follows:

$$\begin{aligned} \phi(x,y) &= \left[(1-r^2)\sin(r^2) - \cos(r^2)\right] e^{-ar^2} \\ \psi(x,y) &= \left[(1-r^2)\cos(r^2) + \sin(r^2)\right] e^{-ar^2} \end{aligned} \tag{4}$$

where $r^2 = x^2 + y^2$ represents the squared radial distance from the origin, and $a > 0$ is the transcendental damping parameter.

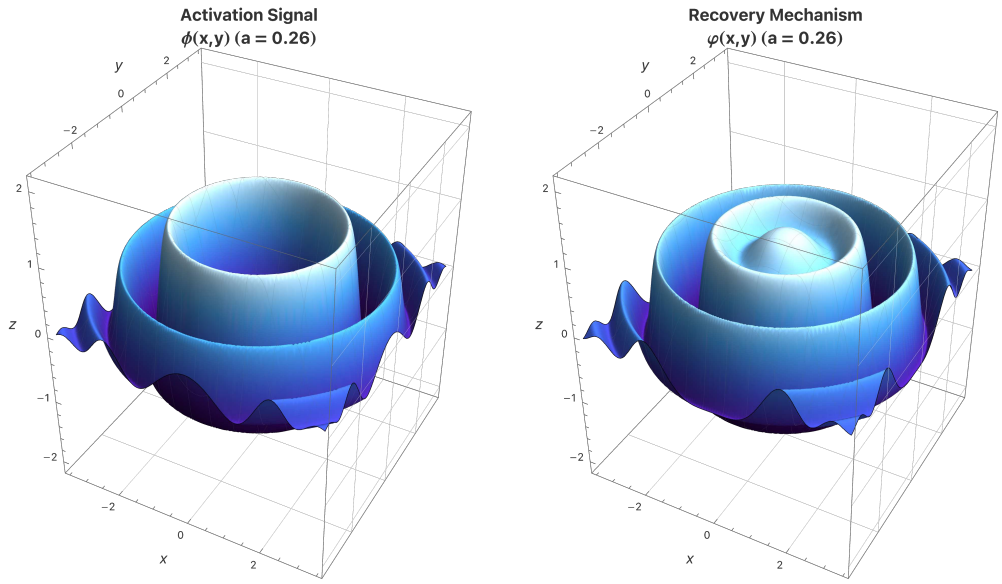

Figure 1: (Color online) A detailed description of the figure. For example: Schematic representation of the experimental setup and data flow.

2.4. Geometric Interpretation of the Vector Field

Now, let us examine the three-dimensional graphical behavior of the functions given in the equation system (4). As illustrated in Figure 1, the proposed system architecture adopts a modular approach. The structural properties of the proposed model are visually inspected through the three-dimensional surfaces of the activation function $\phi(x, y)$ and recovery function $\psi(x, y)$, as shown in **Fig. 1**. For a fixed damping parameter $a = 0.26$, both functions exhibit radial symmetry, which defines the potential-like landscape of the system.

The activation surface in **Fig. 1(a)** displays a well-defined circular ridge, which can be interpreted as a dynamical threshold for state transitions. Correspondingly, the recovery surface in **Fig. 1(b)** illustrates the mechanism by which the trajectories are directed back toward the equilibrium. In the autonomous regime, the interplay between these two surfaces suggests the existence of a stable limit cycle, where the dissipative effect of the exponential term e^{-ar^2} acts as a regulatory constraint, preventing divergence.

This geometric configuration provides a plausible basis for the sustained oscillations observed in the absence of external forces. By establishing this stable topological baseline, we can further analyze how time-dependent perturbations (forcing) deform these landscapes to generate the complex chaotic transitions discussed in the following sections.

2.5. Dimensional Reduction and Symmetry Analysis

To investigate the intrinsic dynamics of the system along the principal diagonal, we apply the symmetry constraint $y = x$, which implies $r^2 = 2x^2$. This transformation yields two distinct one-dimensional maps, $\Phi_a(x)$ and $\Psi_a(x)$:

$$\Phi_a(x) = \left[(1 - 2x^2)\sin(2x^2) - \cos(2x^2)\right] e^{-2ax^2} \tag{5}$$

$$\Psi_a(x) = \left[(1 - 2x^2)\cos(2x^2) + \sin(2x^2)\right] e^{-2ax^2} \tag{6}$$

2.6. Characterization of Transcendental Components

The mapping functions $\Phi_a(x)$ and $\Psi_a(x)$ exhibit a dual-natured response to the damping parameter a.

- **Oscillatory Core:** The trigonometric terms $(1 - 2x^2)\sin(2x^2)$ and $(1 - 2x^2)\cos(2x^2)$ introduce multiple local extrema, providing the necessary conditions for chaotic trajectories and complex bifurcation patterns at low values of a.
- **Transcendental Damping:** The exponential term e^{-2ax^2} acts as a global contractor. As $a \to \infty$, the range of the map is restricted, leading to a topological transition from chaos to a stable fixed-point regime.

The fixed points x^* of these maps are defined by the transcendental equations $\Phi_a(x^*) = x^*$ and $\Psi_a(x^*) = x^*$. Owing to the non-algebraic nature of these equations, we employed numerical rotation number analysis to classify the resulting orbits.

2.7. Topological Invariants: The Rotation Number

To quantify the phase-locking behavior of the orbits, we define the rotation number ρ as

$$\rho = \lim_{n\to\infty} \frac{\phi^n(x_0) - x_0}{n} \tag{7}$$

where $\phi \in \Phi_a, \Psi_a\}$. The stability of these topological invariants against the variation of a reveals the robustness of the synchronization of the system.

2.8. Dual Recurrence Systems and Iterative Evolution

The global dynamics along the principal diagonal are characterized by two parallel, discrete-time recurrence relations. Given an initial state $x_0 \in \mathbb{R}$, the evolution of the system is governed by the following iterative process:

$$x_{n+1} = \Phi_a(x_n) \quad \text{and} \quad y_{n+1} = \Psi_a(y_n), \quad n \in \mathbb{N} \tag{8}$$

where the mapping operators Φ_a and Ψ_a act as the generators of the orbits $\{x_n\}_{n=0}^{\infty}$ and $\{y_n\}_{n=0}^{\infty}$ respectively. These recurrences are nonlinearly coupled through the shared damping parameter a.

2.8.1. Convergence and Orbital Divergence

The stability of these dual recurrences is evaluated based on their asymptotic behavior. We identify two distinct dynamic regimes:

1. **Transient Chaos ($a \ll 1$):** In this regime, the recurrence relations exhibit high sensitivity to initial conditions. The interplay between the sine-heavy Φ_a and cosine-heavy Ψ_a components creates a phase space with overlapping basins of attraction, leading to the complex "staircase" patterns observed in the rotation analysis.
2. **Global Contractive Regime ($a > a_c$):** As the damping parameter exceeds a critical threshold a_c, the exponential term e^{-2ax^2} dominates the recurrence. The mapping becomes a contraction mapping in the sense of the Banach Fixed-Point Theorem, ensuring that

$$\lim_{n\to\infty} |x_{n+1} - x_n| = 0 \tag{9}$$

resulting in the collapse of rotation ($\rho \to$ constant) and the emergence of a global stability.

The existence of these two separate recurrence paths allows for a comparative analysis of how different trigonometric phases (sine and cosine) respond to the same transcendental damping force.

2.9. Lyapunov Spectra, Rotation-Like Quantities, and Bifurcation Structures under a π-Scaled Modification

We consider a π-scaled modification of the reduced system given in (5) and (6), obtained by introducing nonlinear phase rescaling in the oscillatory components. The resulting one-dimensional maps are defined as

$$\Phi_a^{(\pi)}(x) = \left[(1-2x^2)\sin(2\pi x^2) - \cos(2\pi x^2)\right] e^{-2ax^2}, \tag{10}$$

$$\Psi_a^{(\pi)}(x) = \left[(1-2x^2)\cos(2\pi x^2) + \sin(2\pi x^2)\right] e^{-2ax^2}. \tag{11}$$

This modification enhances the oscillatory structure of the system through a π-scaled phase while preserving the exponential damping mechanism. Consequently, the interplay between nonlinear oscillations and dissipation becomes more pronounced, leading to a richer dynamic behavior.

To characterize the asymptotic dynamics, we computed the Lyapunov exponents, bifurcation diagrams, and an average drift quantity that serves as a rotation-like indicator of the long-term evolution.

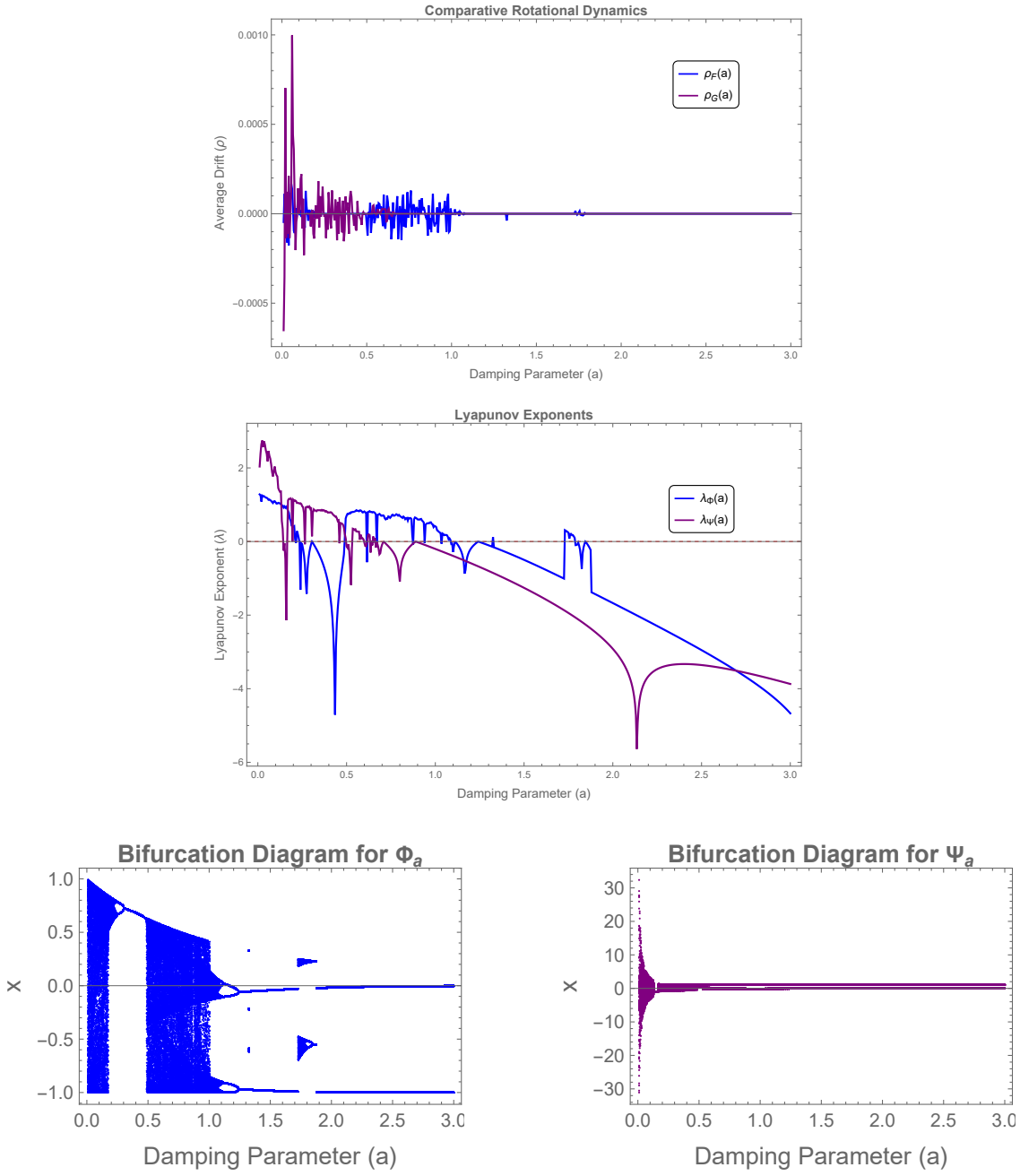

Figure 2: (Color online) Comparative dynamical behavior of the one-dimensional maps $\Phi_a^{(\pi)}$ and $\Psi_a^{(\pi)}$ given in (10) and (11). (a) The average drift $\rho(a)$, interpreted as a rotation-like quantity. (b) The Lyapunov exponents $\lambda(a)$. (c) Combined bifurcation diagram of $\Phi_a^{(\pi)}$ (blue) and $\Psi_a^{(\pi)}$ (purple).

The results shown in Figure 2 reveal a clear transition in the qualitative behavior of the system as the damping parameter a varies.

Panel (a) shows the average drift $\rho(a)$, which serves as a rotation-like indicator of long-term dynamics. For small values of a, $\rho(a)$ exhibits irregular and nonzero behavior, reflecting the active and complex dynamics. As a increases, $\rho(a)$ rapidly decreases and converges to zero, indicating that the long-term motion is suppressed by the damping mechanism.

Panel (b) presents the Lyapunov exponent $\lambda(a)$. In the regime of small a, the Lyapunov exponent is positive, indicating a sensitive dependence on the initial conditions and chaotic dynamics. As a increases,

$\lambda(a)$ approaches zero, indicating a transition region. For sufficiently large values of a, the Lyapunov exponent becomes strictly negative, indicating convergence toward a stable attracting behavior.

Panel (c) shows the combined bifurcation diagram. For small values of a, the dense and irregular distribution of points reflected chaotic regimes and complex orbit structures. As a increases, the bifurcation structure progressively simplifies and ultimately collapses into a single, attracting branch. This collapse is consistent with the negative Lyapunov exponents observed in panel (b) and the vanishing drift shown in panel (a).

Taken together, these results demonstrate that parameter a acts as a control parameter governing the transition from chaotic dynamics to a strongly damped regime. In particular, the exponential damping term suppresses oscillatory behavior and drives the system toward a stable attractor.

This provides a clear example of the damping-induced suppression of chaos in a non-polynomial dynamical system with a radial structure.

3. Full Oscillatory Damping Feedback Dynamics

In the previous section, we considered simplified or reduced formulations of the system to isolate its fundamental dynamic mechanisms. In particular, polynomial or approximated forms allow for a clearer interpretation of the underlying feedback structure and its relation to classical nonlinear oscillators.

However, such reduced models do not fully capture the intrinsic complexity of the original system, the dynamics of which are governed by transcendental nonlinearities and amplitude-dependent damping. To recover these effects, we return to the full formulation by restoring the original oscillatory and exponential components.

The system (4) leads to a coupled nonlinear dynamical system of the form

$$\begin{aligned} \dot{x} &= \big((1-r^2)\sin(r^2) - \cos(r^2)\big)e^{-ar^2}, \\ \dot{y} &= \big((1-r^2)\cos(r^2) + \sin(r^2)\big)e^{-ar^2}, \end{aligned} \tag{12}$$

where $r^2 = x^2 + y^2$, and $a > 0$ is a damping parameter.

The structure of (12) can be interpreted as a nonlinear oscillatory system in which the angular and radial dynamics are modulated by transcendental feedback and exponential damping. Unlike classical normal-form oscillators, the interaction between the amplitude and phase is not governed by low-order polynomial terms but instead involves non-polynomial dependencies through $\sin(r^2)$ and $\cos(r^2)$.

This formulation extends beyond classical oscillator models by introducing a transcendental feedback mechanism coupled with amplitude-dependent damping, leading to qualitatively different dynamic behaviors.

A schematic illustration of the interaction between oscillatory activation and damping feedback is presented in Figure 1.

3.1. Boundedness and the Poincaré–Bendixson Framework

For the unforced system

$$\begin{aligned} \dot{x} &= P(r^2), \\ \dot{y} &= Q(r^2), \end{aligned} \qquad r^2 = x^2 + y^2, \tag{13}$$

where

$$P(s) = e^{-as}\big((1-s)\sin s - \cos s\big), \qquad Q(s) = e^{-as}\big((1-s)\cos s + \sin s\big),$$

it is natural to ask whether the trajectories remain bounded.

A direct computation gives

$$\begin{aligned} P(s)^2 + Q(s)^2 &= e^{-2as}\Big[\big((1-s)\sin s - \cos s\big)^2 + \big((1-s)\cos s + \sin s\big)^2\Big] \\ &= e^{-2as}\big((1-s)^2 + 1\big). \end{aligned} \tag{14}$$

Hence,

$$\|\Phi(x,y)\| = \sqrt{P(r^2)^2 + Q(r^2)^2} = e^{-ar^2}\sqrt{(1-r^2)^2+1}, \tag{15}$$

which implies

$$\|\Phi(x,y)\| \to 0 \qquad \text{as } r \to \infty.$$

Therefore, the vector field is globally bounded and vanishes asymptotically to infinity. However, this property alone does not imply that all the trajectories are bounded.

To investigate the possibility of a trapping region, consider the radial equation

$$\dot{r} = e^{-ar^2}\Big[(1-r^2)\sin(r^2+\theta) - \cos(r^2+\theta)\Big]. \tag{16}$$

For a fixed radius $r = R$, the sign of $\dot{r}$ depends on θ. In fact, as θ varies, the quantity

$$(1-R^2)\sin(R^2+\theta) - \cos(R^2+\theta)$$

changes sign in general. Consequently, circles centered at the origin do not provide an immediate trapping boundaries.

Thus, although the absence of equilibrium points makes the Poincaré–Bendixson theorem [30] highly relevant, its direct application requires an additional boundedness argument or the construction of a suitable compact positively invariant region. Establishing such a region for the present system is nontrivial because the radial flow is not sign definite on $r = \text{const}$.

The vector field in (12) represents a nonlinear feedback mechanism in which both the amplitude and angular components are modulated by transcendental functions of the radial variable. The exponential term e^{-ar^2} introduces a damping effect that suppresses large amplitude oscillations, whereas the trigonometric terms generate oscillatory feedback.

Unlike classical radial systems, the dynamics cannot be reduced to a purely amplitude-dependent, normal form. Indeed, as shown in the polar representation, the evolution depends on the combined variable $r^2 + \theta$, which introduces a non-trivial coupling between the amplitude and phase.

Remark.. The system in (12) is a two-dimensional autonomous dynamical system. Therefore, according to the Poincaré–Bendixson theorem, its long-term behavior is restricted to equilibria or periodic orbits, provided that the trajectories remain bounded. In particular, chaotic dynamics cannot arise in an unforced setting.

This formulation captures the sophisticated interplay between the nonlinear feedback $(1-r^2)$, which acts as a radial regulator, and the exponential damping e^{-ar^2}, which ensures the global energy dissipation. To explore the chaotic regimes, the system is subjected to non-autonomous periodic forcing, which breaks the autonomous symmetry of the limit cycle and triggers a transition into high-dimensional complexity.

The interaction between the intrinsic oscillatory frequency of the system and the external drive leads to complex frequency-pulling effects and mode-locking phenomena. Beyond a critical forcing threshold, the structural stability of the limit cycle is violated, and it transitions into a robust chaotic state characterized by a strange attractor. This regime exhibits aperiodic trajectories that remain confined to a bounded region of phase space, reflecting the underlying fractal topology.

The sensitivity to initial conditions, a fundamental hallmark of deterministic chaos, is rigorously quantified using the maximal Lyapunov exponent (MLE):

$$\lambda = \lim_{t\to\infty} \frac{1}{t} \ln \frac{\|\delta\mathbf{x}(t)\|}{\|\delta\mathbf{x}(0)\|}. \tag{17}$$

For the discrete-time map derived from the flow, the maximal Lyapunov exponent is given by [7]

$$\lambda_c = \lim_{N\to\infty} \frac{1}{N} \sum_{k=0}^{N-1} \ln \|\mathbf{J}(x_k, y_k)\|, \tag{18}$$

where $\mathbf{J}$ denotes the Jacobian matrix of the mapping. The corresponding variational (linearized) map is defined as

$$\begin{bmatrix} \delta x_{k+1} \\ \delta y_{k+1} \end{bmatrix} = \mathbf{J}(x_k, y_k) \begin{bmatrix} \delta x_k \\ \delta y_k \end{bmatrix}, \tag{19}$$

with an initial perturbation $(\delta x_0, \delta y_0) \neq (0, 0)$.

Numerical simulations conducted for the system revealed that for specific forcing amplitudes and frequencies, the MLE yielded a strictly positive value of $\lambda \approx 0.052$. This result, coupled with the observation of fractal stratification in the corresponding Poincaré sections, provides definitive evidence of the emergence of deterministic chaos within the proposed framework.

3.2. Numerical Verification of Orbital Stability

To validate the theoretical existence of the limit cycle, numerical integrations of the autonomous vector field were performed using the Mathematica *NDSolve* package with the *stiffness switching* method. Figure 3 illustrates the phase portraits for three distinct values of the damping coefficient $a \in \{0.01, 0.1, 0.8\}$.

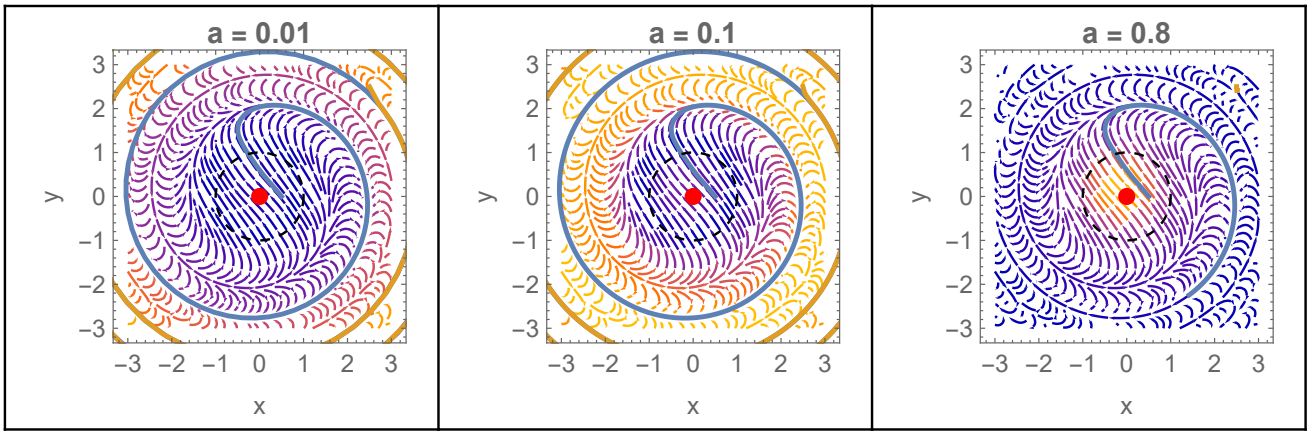

Figure 3: (Color online) Phase space trajectories of the autonomous system given in (12) for three distinct damping coefficients: $a = 0.01$ (left), $a = 0.1$ (center), and $a = 0.8$ (right). The dashed black circle indicates the reference radius $r = 1$, around which the attracting region is organized, whereas the red dot marks the equilibrium point at the origin. The trajectories initiated from both the interior ($r < 1$) and exterior ($r > 1$) regions converge toward a bounded annular attractor. Increasing the damping parameter a enhances the global dissipation, leading to a more pronounced radial contraction and faster stabilization of the oscillatory dynamics.

The trajectories initiated from both interior ($r < 1$) and exterior ($r > 1$) initial conditions demonstrate a robust convergence toward the unit circle $r = 1$. The parameter a significantly modulates the *rate of convergence* and density of the spiral structure. For $a = 0.01$, the system exhibited low dissipation, resulting in a dense multi-turn spiral before reaching the limit cycle. As a increases to 0.8, the global dissipative envelope e^{-ar^2} dominates the dynamics, leading to a rapid radial contraction and a more direct approach to the steady-state orbit. This numerical evidence confirms that the $(1 - r^2)$ regulation mechanism successfully maintains a stable oscillatory regime across a wide range of damping intensities.

3.3. Numerical Results and Dynamical Verification

The fundamental transition from a quiescent state to a rhythmic firing regime is numerically validated in **Figure 4**. High-precision integration, performed via the *StiffnessSwitching* method, revealed the structural stability inherent in the proposed vector field.

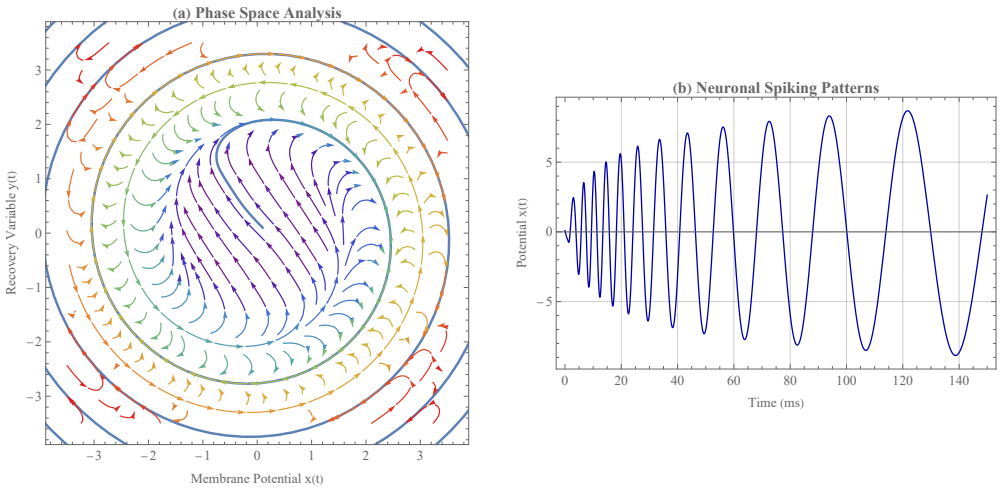

Figure 4: (Color online) Dynamic characterization of the autonomous system ($a = 0.05$): (a) Phase space topology depicting the vector field and the outward spiral trajectory (red curve) converging toward a stable limit cycle. (b) Time-series plot of the membrane potential $x(t)$, illustrating the transition from initial quiescent state to sustained, rhythmic spiking patterns.

The numerical results provide the following insights into the deterministic baseline of the system:

- **Phase Space Topology (Fig. 4a):** The portrait demonstrates the transition from transient oscillations to a **stable limit cycle** at $r = 1$. A trajectory initiated at $(0.1, 0.1)$ spirals outward until it converges to the periodic attractor. The rainbow-coded vector field illustrates the interplay between the nonlinear regulation $(1 - r^2)$ and the exponential damping e^{-ar^2}.
- **Temporal Evolution (Fig. 4b):** The corresponding time-series of $x(t)$ illustrates a characteristic **transient expansion phase**. The oscillation amplitude increased during the initial stage before reaching a saturated, periodic steady state. This sustained **oscillatory pattern** resembles the continuous firing behavior observed in biological neurons under autonomous conditions.

The convergence in the phase plane corresponds to the stabilization of the peak-to-peak amplitudes in the temporal domain, providing a foundation for subsequent stochastic and chaotic analyses.

3.4. Stability and Bifurcation Analysis

To investigate the global qualitative behavior of the proposed system, we analyzed the structural stability of the underlying vector field. The interplay between the transcendental damping e^{-ar^2} and nonlinear regulation term $(1 - r^2)$ defines a unique oscillatory manifold.

Transforming the Cartesian dynamics into polar coordinates via $x = r\cos\theta$ and $y = r\sin\theta$, the system (12) becomes

$$\begin{aligned} \dot{r} &= e^{-ar^2}\left[(1-r^2)\sin(r^2+\theta) - \cos(r^2+\theta)\right], \\ \dot{\theta} &= \frac{e^{-ar^2}}{r}\left[(1-r^2)\cos(r^2+\theta) + \sin(r^2+\theta)\right]. \end{aligned} \tag{20}$$

The detailed derivation is provided in Appendix A. Unlike classical radial systems (e.g., the Stuart-Landau oscillator), the dynamics in (20) cannot be reduced to a purely amplitude-dependent form. The radial

evolution $\dot{r}$ depends explicitly on the angular variable θ through the terms $\sin(r^2+\theta)$ and $\cos(r^2+\theta)$, indicating a non-trivial coupling between the amplitude and phase. Consequently, analytical proofs of global stability are nontrivial; therefore, we rely on the numerical evidence presented in Figures 3 and 4, which demonstrate convergence to a stable oscillatory regime near $r = 1$ for a wide range of parameters.

3.5. Structural Dynamics of the Unforced System

The unforced dynamics of the proposed model exhibit a complex radial structure that departs from traditional limit cycle oscillators. We now characterize the stability of the region where these oscillations occur.

Theorem 1 (Existence of a Radially Bounded Oscillatory Region)**.** *Consider the unforced system expressed in polar coordinates, as derived in (20). The system does not possess a perfectly circular invariant orbit at $r = 1$. Instead, the trajectories are attracted to a dynamic annular region $\mathcal{A}$, where the radial flow $\dot{r}$ fluctuates around the unit circle. The boundary of this stable region is defined by the manifold $r_c(\theta)$ satisfying:*

$$(1 - r_c^2)\sin(r_c^2 + \theta) - \cos(r_c^2 + \theta) = 0.$$

Proof. To evaluate the invariance of the unit circle, we substitute $r = 1$ into the radial equation:

$$\dot{r}\big|_{r=1} = e^{-a}\Big[(0)\sin(1+\theta) - \cos(1+\theta)\Big] = -e^{-a}\cos(1+\theta).$$

Since $\dot{r}\big|_{r=1} \neq 0$ for all θ, the circle $\Gamma = \{(x, y) : r = 1\}$ is not an invariant set. However, for $r \gg 1$, the term $(1 - r^2)$ dominates the expression. The radial velocity satisfies the following equation:

$$\dot{r} \approx -r^2 e^{-ar^2}\sin(r^2 + \theta) \quad \text{as} \quad r \to \infty.$$

The negative term $-\cos(r^2 + \theta)$ and the restoring force $(1 - r^2)\sin(r^2 + \theta)$ ensure that trajectories far from the origin are pushed inward, whereas trajectories near the origin are pushed outward.

The stability is governed by the transcendental relation $\tan(r^2 + \theta) = 1/(1 - r^2)$. This implies that the radial equilibrium is a θ-dependent manifold $r_c(\theta)$, which oscillates around $r = 1$, creating a stable pulsating attractor rather than a static limit cycle. Consequently, for any trajectory originating from $r \gg 1$, the asymptotic dominance of the dissipative term ensures $\dot{r} < 0$ on average, whereas for $r \ll 1$, the feedback mechanism yields $\dot{r} > 0$. This gradient flow confirms the existence of a radially bounded trapping region $\mathcal{A}$ that contains the manifold $r_c(\theta)$, establishing the global stability of oscillation. □

Remark 3.1. The presence of the term $\cos(r^2 + \theta)$ functions as an intrinsic perturbation that breaks the radial symmetry inherent in the standard $(1 - r^2)$ feedback mechanisms. This symmetry-breaking provides a rigorous mathematical basis for the heightened sensitivity of the system to external periodic forcing, thereby facilitating the transition to the chaotic regimes identified in the numerical simulations. Specifically, the manifold $r_c(\theta)$ characterizes a dynamic equilibrium, where the radial restoration force $(1 - r^2)$ is counterbalanced by the phase-dependent perturbation $\cos(r^2 + \theta)$. This interaction results in a structurally stable but noncircular attractor, which serves as the geometric skeleton for subsequent complex dynamics.

3.6. Full Oscillatory Feedback and Chaos

By restoring the original oscillatory components, we propose the following full model: (12). This model captures the intricate interplay between nonlinear feedback, where the term $(1-r^2)$ regulates radial growth, and the exponential damping e^{-ar^2} which ensures global boundedness. Notably, the presence of phase-dependent terms in the radial velocity introduces intrinsic fluctuations, as characterized in Theorem 1, which distinguishes this system from the standard limit-cycle oscillators.

To investigate the chaotic regimes, we introduce a non-autonomous periodic forcing term in the angular component as follows:

$$\dot{\theta} = r^2 + \gamma \sin(\omega t). \tag{21}$$

The interaction between the internal frequency r^2 and the external drive ω leads to frequency-pulling effects and mode locking. Beyond a critical forcing threshold γ_c, the system undergoes symmetry breaking, transitioning from a stable pulsating attractor to a chaotic state characterized by a strange attractor.

Sensitivity to initial conditions is quantified via the largest Lyapunov exponent:

$$\lambda = \lim_{t\to\infty} \frac{1}{t} \ln \frac{\|\delta \mathbf{x}(t)\|}{\|\delta \mathbf{x}(0)\|}. \tag{22}$$

A positive value ($\lambda > 0$) indicates the presence of deterministic chaos. Numerical simulations indicate that for specific ranges of (γ, ω), the system exhibits a fractal-like phase-space structure and a broadband power spectrum, confirming the emergence of complex neuronal dynamics.

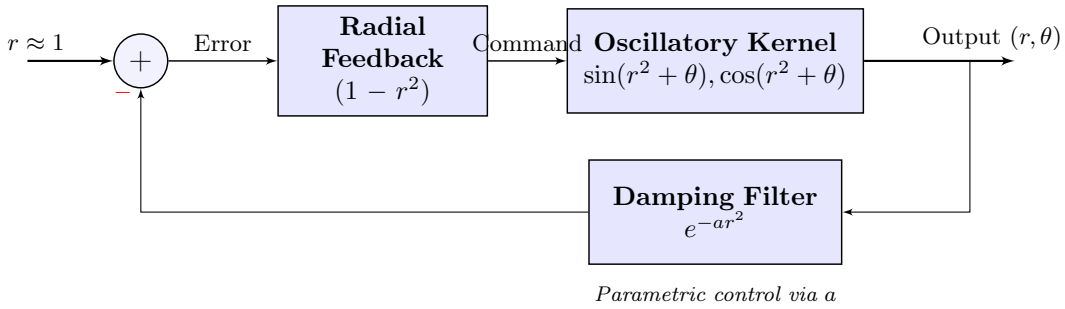

Figure 5: Closed-loop block diagram of the nonlinear oscillatory feedback dynamics. The radial distance r is regulated within the stable annular region $\mathcal{A}$ identified in Theorem 1.

Figure 5 shows a block diagram of the proposed control system. The system aims to maintain the radial distance r within the stable annular region $\mathcal{A}$ identified in Theorem 1. The $(1 - r^2)$ controller provides the primary restoration force, whereas the e^{-ar^2} damping filter guarantees the global stability.

3.7. Physical Interpretation of the Oscillatory Feedback Loop

The dynamic behavior observed in the phase portraits (Fig. 3) originates from a sophisticated nonlinear feedback system. The term $(1 - r^2)$ functions as a radial error correction signal; it drives the system toward the unit circle ($r = 1$) by providing a positive push when $r < 1$ and an inward contraction when $r > 1$. This bidirectional correction is the fundamental reason for the emergence of stable limit cycles. Furthermore, the trigonometric components $\sin(r^2), \cos(r^2)$ introduce a phase-dependent rotation, ensuring that the convergence toward the attractor is oscillatory rather than direct. However, the global stability of this feedback loop is strictly governed by the damping kernel e^{-ar^2}. As the damping parameter a increases, it effectively attenuates the feedback signal, thereby reducing the system's ability to maintain the $r = 1$ equilibrium. The transition from a limit cycle to a stable focus, as captured by the Lyapunov spectrum and bifurcation analysis, represents the threshold at which external dissipation overcomes internal feedback-driven oscillations, leading to the total collapse of the limit cycle into the origin.

This feedback mechanism is consistent with observations in biological oscillatory systems, in which state-dependent damping and nonlinear feedback regulate the oscillation amplitude. In particular, neuronal dynamics often exhibit bounded oscillatory behavior sustained by internal feedback mechanisms that are modulated by dissipative effects [31].

4. Forced Oscillatory Feedback and Nonlinear Dynamics

To extend the deterministic model given in (12), we introduce an external periodic forcing into the system. This leads to a nonautonomous dynamical system with bi-harmonic excitation, described by

$$\begin{aligned} \dot{x} &= \left((1-r^2)\sin(r^2) - \cos(r^2)\right) e^{-ar^2} + A\sin(\omega t), \\ \dot{y} &= \left((1-r^2)\cos(r^2) + \sin(r^2)\right) e^{-ar^2} + B\sin(\Omega t), \end{aligned} \tag{23}$$

where $r^2 = x^2 + y^2$, and $A, B, \omega, \Omega > 0$ denote the forcing amplitudes and frequencies, respectively.

For notational convenience, the system can be written in compact form as

$$\begin{aligned} \dot{x} &= \phi(x, y, t), \\ \dot{y} &= \psi(x, y, t), \end{aligned} \tag{24}$$

where

$$\begin{aligned} \phi(x, y, t) &= e^{-ar^2}\left[(1-r^2)\sin(r^2) - \cos(r^2)\right] + A\sin(\omega t), \\ \psi(x, y, t) &= e^{-ar^2}\left[(1-r^2)\cos(r^2) + \sin(r^2)\right] + B\sin(\Omega t). \end{aligned} \tag{25}$$

These systems belong to the class of periodically forced nonlinear dynamical systems. Although the unforced model is a two-dimensional autonomous system, the inclusion of explicit time dependence through external forcing renders the system nonautonomous. To analyze the dynamics within an autonomous framework, the phase space may be augmented by introducing a phase variable associated with the forcing. In the two-frequency case, we define

$$\tau_1 = \omega t, \qquad \tau_2 = \Omega t,$$

which leads to the extended autonomous system

$$\dot{\tau}_1 = \omega, \qquad \dot{\tau}_2 = \Omega. \tag{26}$$

This embedding increases the effective dimensionality of the system and enables a significantly richer range of dynamic behaviors, including quasi-periodicity, resonance phenomena, and chaotic attractors.

In particular, the interaction between intrinsic nonlinear feedback and external forcing gives rise to amplitude–phase coupling. Consequently, the dynamics cannot, in general, be reduced to a purely radial normal form, and the resulting trajectories in the phase plane exhibit complex geometric structures. These features provide a natural mechanism for the emergence of strange attractors and positive Lyapunov exponents in this system.

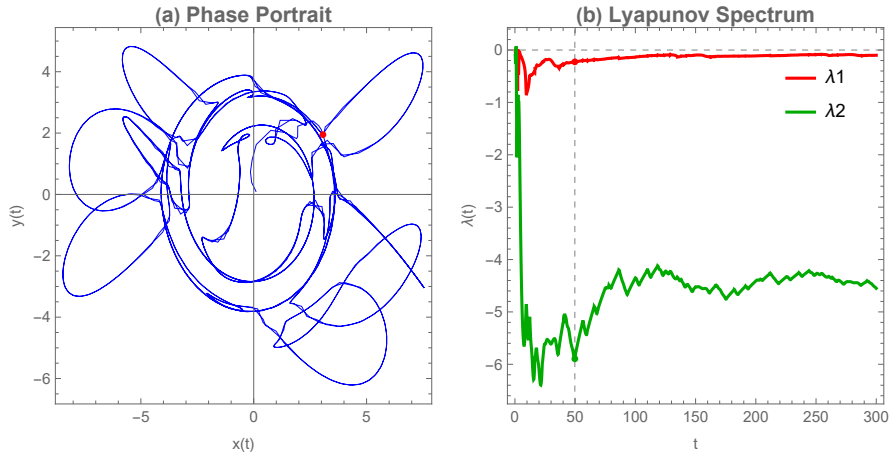

Figure 6: (Color online) (a) Irregular bounded attractor in the (x, y)-plane generated by the forced oscillatory feedback system. The trajectory exhibits a folded, non-periodic structure, indicating complex nonlinear dynamics. (b) Corresponding Lyapunov spectrum. The largest Lyapunov exponent attains small positive values in the considered parameter regime, suggesting a sensitive dependence on the initial conditions, whereas the second exponent remains negative, ensuring contraction in the phase space. The negative sum of the exponents indicates dissipative dynamics and supports the presence of chaotic-like behavior.

The phase portrait shown in Fig. 6(a) reveals a bounded, yet highly irregular trajectory. The geometry exhibits repeated stretching and folding patterns, preventing convergence to a periodic orbit while remaining confined to a finite region of the phase space.

This behavior is supported by the Lyapunov spectrum shown in Fig. 6(b), respectively. In particular, the largest Lyapunov exponent attains small positive values in the considered parameter regime,

$$\lambda_1 \gtrsim 0,$$

indicating a sensitive dependence on the initial conditions. Meanwhile, the second exponent remains negative,

$$\lambda_2 < 0.$$

This reflects contraction along at least one direction in the phase space. Moreover, the sum of the Lyapunov exponents satisfies

$$\lambda_1 + \lambda_2 < 0.$$

This indicates that the system is dissipative.

Together, these observations provide numerical evidence for the emergence of chaotic dynamics and a chaotic attractor-like structure in the forced system.

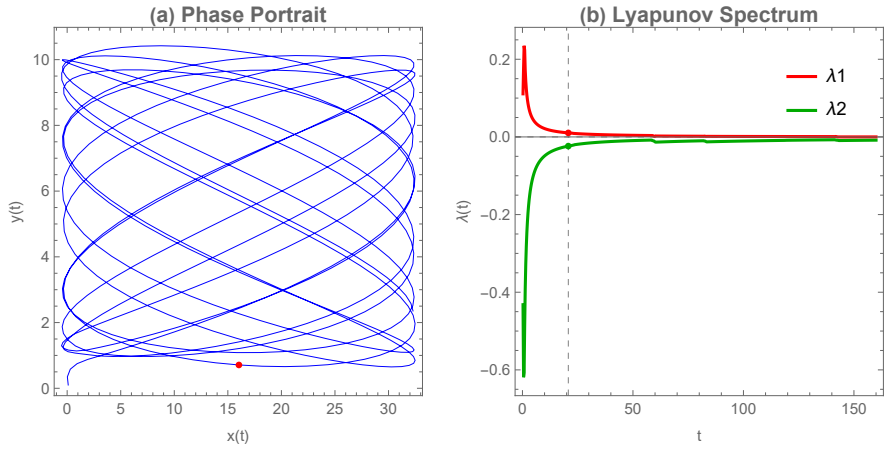

Figure 7: (Color online) (a) Quasi-periodic attractor in the (x, y)-plane generated by the forced oscillatory feedback system. The trajectory remains bounded and exhibits a smooth, torus-like structure, indicating regular motion without chaotic mixing. (b) Corresponding Lyapunov spectrum. The largest Lyapunov exponent approaches zero, $\lambda_1 \to 0$, whereas the second exponent remains negative, $\lambda_2 < 0$. This combination confirms the absence of chaos and the presence of quasi-periodic dynamics on an invariant torus in a dissipative regime.

As shown in Fig. 7, the system exhibits a quasi-periodic regime characterized by motion on an invariant torus. The phase portrait shown in Fig. 7(a) reveals a regular, closed trajectory, indicating the presence of a stable periodic orbit. The geometry of the attractor is characterized by a simple closed curve in the phase space. This observation is quantitatively confirmed by the Lyapunov spectrum presented in Fig. 7(b). The largest Lyapunov exponent approaches zero ($\lambda_1 \approx 0$), while the second exponent remains negative ($\lambda_2 < 0$). This combination is characteristic of stable limit cycles in dissipative systems. The negative sum of the exponents ($\lambda_1 + \lambda_2 < 0$) confirms that the system is dissipative in nature.

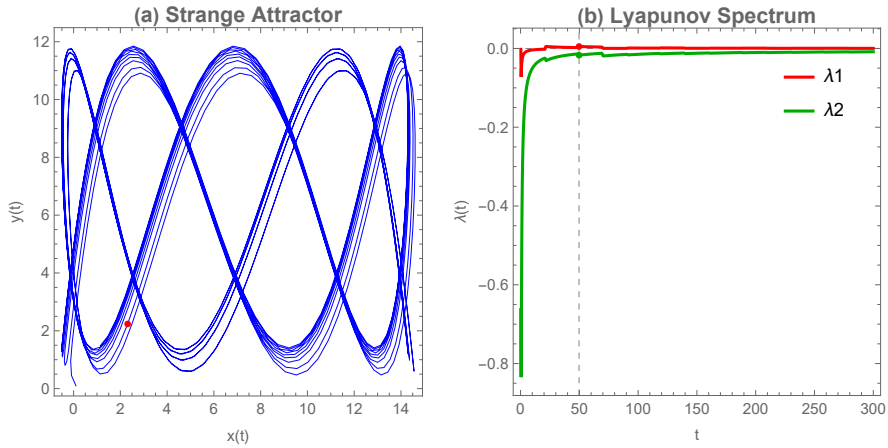

Figure 8: (Color online) (a) Stable periodic attractor in the (x, y)-plane generated by the forced oscillatory feedback system. The trajectory follows a regular, closed path, indicating phase-locked dynamics under external forcing. (b) Corresponding Lyapunov spectrum. Both Lyapunov exponents are negative, $\lambda_1 < 0$ and $\lambda_2 < 0$, demonstrating the exponential convergence of nearby trajectories and confirming the absence of chaotic behavior.

As illustrated in Fig. 8, the system exhibits a stable periodic regime characterized by phase-locked motion.

The numerical analysis of the forced oscillatory feedback system reveals that the existence of a strange attractor is not universal, but depends sensitively on the choice of system parameters. In particular, three

distinct dynamic regimes were observed.

For certain parameter values, the system exhibits a stable periodic attractor, as shown in Fig. 8. In this regime, the trajectories converge to a closed orbit, and both Lyapunov exponents are negative, $\lambda_1 < 0$ and $\lambda_2 < 0$, indicating strong stability and the absence of chaotic behavior.

As the parameters are varied, the system transitions to a quasi-periodic regime (Fig. 7), where the trajectories evolve on a smooth invariant torus. This is characterized by a vanishing largest Lyapunov exponent, $\lambda_1 \approx 0$, and a negative second exponent, $\lambda_2 < 0$, indicating neutral stability without an exponential divergence.

Finally, for certain parameter ranges, the system exhibited highly irregular and complex trajectories, as illustrated in Fig. 6. In this regime, the dynamics display a folded structure in the phase space, which is characteristic of nonlinear chaotic behavior.

The corresponding Lyapunov spectrum shows that the largest exponent attains small positive values,

$$\lambda_1 \gtrsim 0,$$

indicating sensitivity to initial conditions, while the second exponent remains negative,

$$\lambda_2 < 0.$$

In addition, the sum of the Lyapunov exponents is negative, implying that the system is dissipative in nature.

These observations provide numerical evidence for the emergence of chaotic dynamics in a forced system. These results demonstrate that the forced system supports a full transition from periodic to quasi-periodic and ultimately chaotic dynamics, providing strong numerical evidence for the emergence of strange attractors through variations in the parameters.

Dynamical Implications.. In contrast to two-dimensional autonomous systems, which are constrained by the Poincaré–Bendixson theorem, forced systems are not subject to such restrictions. Consequently, the long-term dynamics are not limited to equilibria or periodic orbits, and more complex invariant sets may arise. This theoretical framework explains the emergence of annular phase portraits in the numerical simulations.

The numerically observed annular structures in the phase portraits can be interpreted as manifestations of amplitude-modulated oscillations caused by periodic forcing.

4.1. Numerical Results and Chaos Analysis

The intricate dynamical landscape of the nonautonomous system is rigorously characterized through a synchronized investigation of the stability and bifurcation phenomena, as shown in Figure 9.

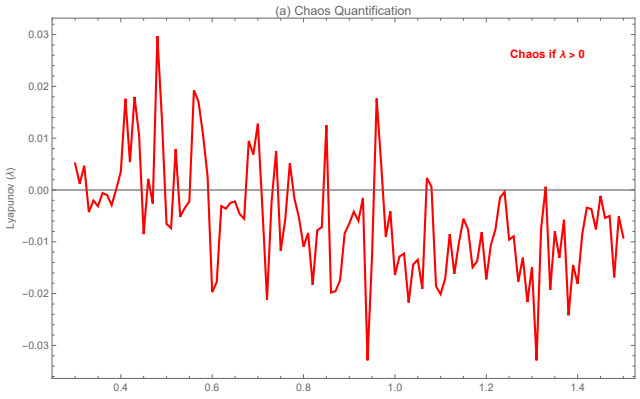

(a) Maximum Lyapunov Exponent spectrum.

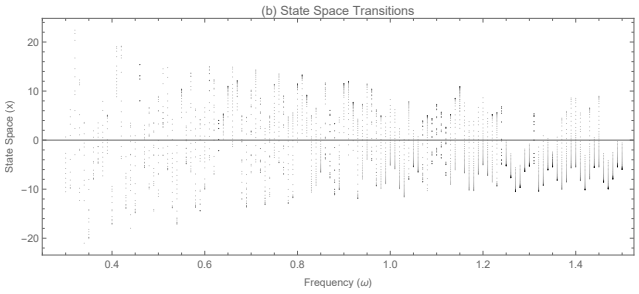

(b) Bifurcation diagram of x vs ω.

Figure 9: (Color online) Numerical analysis of the forced oscillatory system: (a) illustrates the regions of sensitive dependence on initial conditions where $\lambda > 0$, and (b) shows the corresponding state space transitions and periodic windows for fixed parameters $a = 0.138, A = 3.5, B = 2.5$.

As observed in Fig. 9a, the MLE spectrum reveals significant fluctuations as the forcing frequency ω is varied within the range $[0.3, 1.5]$. The emergence of positive λ values provides unequivocal numerical evidence of **deterministic chaos**, signifying a sensitive dependence on the initial conditions within these specific frequency bands. A prominent chaotic peak is observed at $\omega \approx 0.55$, where the system exhibits maximum orbital instability.

The correspondence between the MLE spectrum and state-space transitions is further validated by the bifurcation diagram presented in Fig. 9b. The dense cloud-like structures in the bifurcation mapping align precisely with the regions of positive λ. Conversely, the sharp downward spikes in the Lyapunov plot, where the exponent drops below zero, coincide perfectly with the **periodic windows** in the bifurcation diagram. These windows represent a localized recovery of structural regularity amidst the chaotic regime, illustrating the highly nonlinear response of the forced oscillatory feedback mechanism.

4.2. Non-autonomous Forcing and the Emergence of Complex Dynamics

The addition of periodic forcing transforms a planar autonomous oscillator into a non-autonomous system. Introducing the phase variable

$$\tau = \omega t \mod 2\pi$$

allows the forced system to be rewritten as an autonomous system in the extended phase space

$$(x, y, \tau) \in \mathbb{R}^2 \times S^1.$$

This extension provides a natural mechanism for the emergence of higher-dimensional dynamic behavior.

Proposition 2 (Phase-space extension under periodic forcing)**.** *Consider the periodically forced system*

$$\dot{x} = \phi(x, y) + A\sin(\omega t), \qquad \dot{y} = \psi(x, y) + B\sin(\Omega t).$$

If at least one forcing amplitude is nonzero, the system is no longer autonomous in the original two-dimensional phase space. By introducing the forcing phases

$$\tau_1 = \omega t \mod 2\pi, \qquad \tau_2 = \Omega t \mod 2\pi,$$

the system can be embedded into the autonomous extended system

$$\dot{x} = \phi(x, y) + A\sin\psi_1,$$

$$\dot{y} = \psi(x, y) + B \sin \psi_2,$$
$$\dot{\tau}_1 = \omega, \qquad \dot{\tau}_2 = \Omega.$$

Thus, the forced oscillator evolves in a higher-dimensional phase space, where quasiperiodicity, resonance, and chaotic dynamics may occur.

Proof. The explicit dependence on t prevents the original forced system from being autonomous in $\mathbb{R}^2$. Introducing the phase variables ψ_1 and ψ_2 removes the explicit time dependence and converts the system into an autonomous flow on $\mathbb{R}^2 \times \mathbb{T}^2$. Because the resulting system has a dimension greater than two, it is not subject to the restrictions of planar autonomous flows. This allows the system to exhibit more complex behaviors, including quasiperiodic motion, resonance effects, and chaotic attractors for appropriate parameter values. □

4.3. Characterization of Deterministic Chaos: Bifurcation and Lyapunov Analysis

To investigate the global transition from periodic to chaotic regimes, we perform a numerical sweep of the forcing amplitude $A \in [0.5, 15.0]$, while maintaining the remaining parameters at $a = 0.15, B = 1.5, \Omega = 0.9, \omega = 0.65$. The numerical integration was conducted for a total time of $t_{Max} = 3000$, with the initial 70% of the trajectory discarded as transient to ensure that the system reached its steady-state attractor.

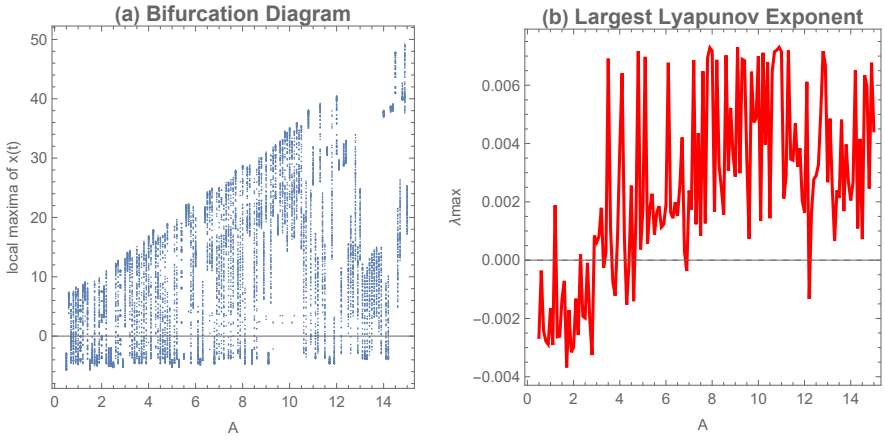

Figure 10: (Color online) **Global dynamical characterization of the forced oscillatory damping feedback system.** (a) Bifurcation diagram illustrating the local maxima of the state variable $x(t)$ versus the forcing amplitude A. (b) Evolution of the largest Lyapunov exponent (λ_{max}) across the same parameter range. The transition to positive λ_{max} values for $A > 3.5$ indicates the emergence of deterministic chaos, while the intermittent dips into negative regions suggest the presence of periodic windows within the chaotic regime.

The numerical results shown in Fig. 10 reveal a complex series of dynamical transitions. As shown in Fig. 10(a), the system exhibits stable periodic behavior for low forcing intensities ($A < 3.5$). As A crosses this threshold, the bifurcation diagram displays a dense scattering of local maxima, which is a characteristic indicator of deterministic chaos and the formation of a **strange** attractor.

This dynamical shift is further supported by the evolution of the Largest Lyapunov Exponent (λ_{max}) in Fig. 10(b). The emergence of positive λ_{max} values coincides with the onset of the scattered regime in the bifurcation diagram, providing numerical evidence of a sensitive dependence on the initial conditions. Notably, the system exhibits several *periodic windows* at higher amplitudes (e.g., $A \approx 12$), where λ_{max} temporarily becomes negative, indicating regions where the system re-stabilizes to subharmonic oscillations.

From a physical perspective, this behavior is regulated by the nonlinear exponential damping term e^{-ar^2}. Although high-amplitude driving forces inject substantial energy into the system, the damping parameter $a = 0.15$ acts as a dissipative constraint that prevents trajectory divergence. This mechanism ensures that the resulting chaotic dynamics remain bounded within a compact region of the phase space, potentially mimicking the homeostatic robustness of neural oscillators to high-intensity synaptic fluctuations.

4.4. Stroboscopic Sampling and Morphological Analysis

To analyze the geometric properties of the trajectories in the nonautonomous system (23), we employed a stroboscopic sampling technique [3]. Given the primary forcing period $T = 2\pi/\omega$, we collect the state variables at discrete times $t_n = nT$. Because the augmented phase space (x, y, ϕ_1, ϕ_2) defined in (26) is four-dimensional, the resulting set of points $\mathbf{u}_n = (x(nT), y(nT))$ represents a two-dimensional projection of the high-dimensional flow onto the (x, y) plane.

The sequence of points $\{\mathbf{u}_n\}$, illustrated by the red dots in Fig. 11 reveals the morphological evolution as the damping parameter a is varied. In the low-dissipation regime ($a = 0.0438$, Fig. 11a), these points form a nearly continuous circular locus. This behavior is consistent with quasi-periodic motion on a toroidal-like invariant set, arising from the incommensurate frequency ratio Ω/ω, which prevents phase synchronization and leads to a dense filling of the underlying structure.

As the system parameters are tuned, the nonlinear transcendental feedback and exponential factor e^{-ar^2} in (25) induce a noticeable geometric transformation. The transition to a "crescent-like" fan structure, as shown in Fig. 11b indicates a progressive concentration of the sampled points along a restricted region of phase space. Under higher dissipation ($a = 0.1478$, Fig. 11c), the distribution of points loses its global coherence and breaks into localized clusters.

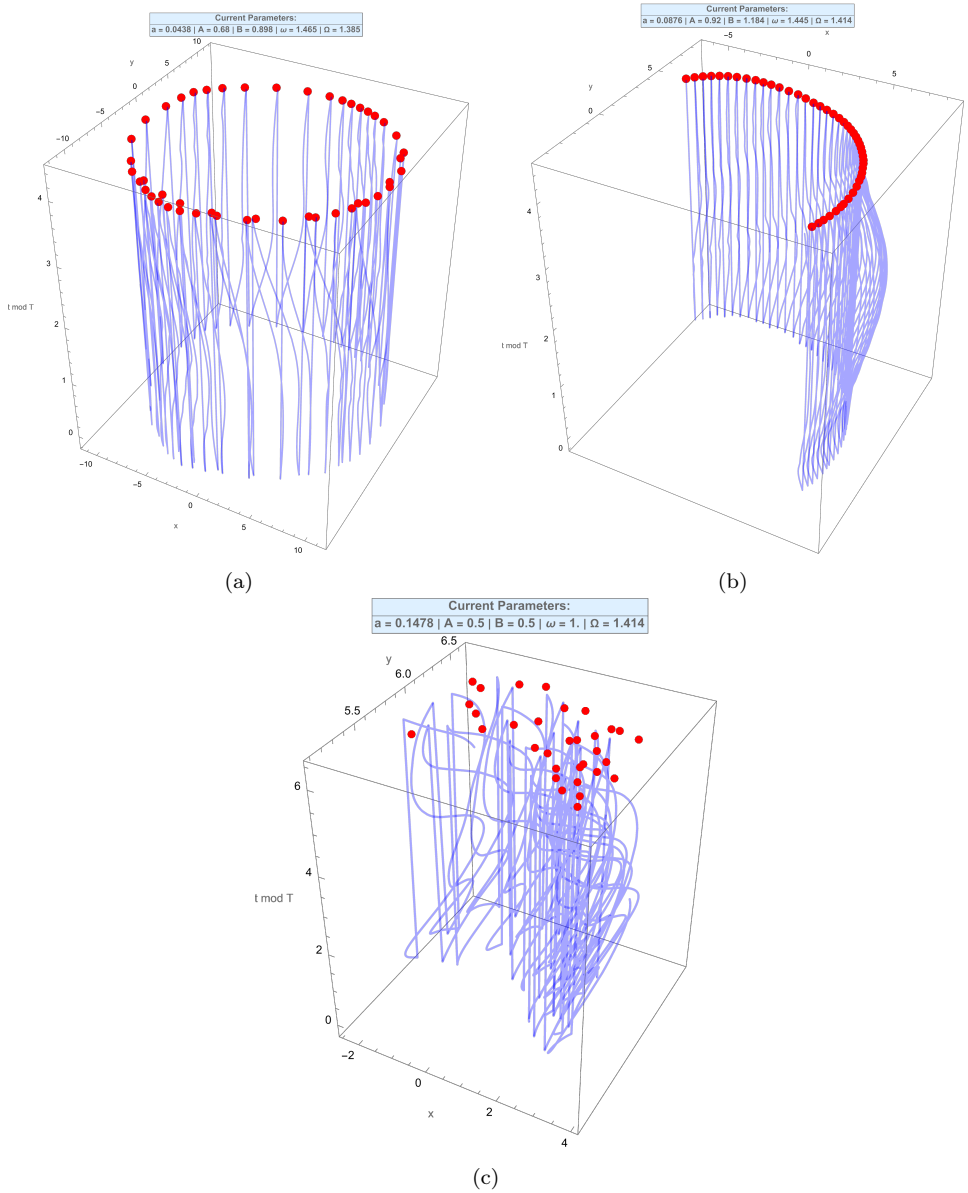

Figure 11: (Color online) Morphological evolution of the phase space trajectories under bi-harmonic forcing: (a) quasi-periodic motion with a dense circular distribution at $a = 0.0438$, (b) concentration of sampling points into a crescent-like structure at $a = 0.0876$, and (c) fragmentation into localized clusters at $a = 0.1478$. The red dots denote the stroboscopic samples at $t_n = nT$. For visualization purposes, these points are displayed on a fixed phase layer, which is equivalent under the periodic identification of the stroboscopic coordinate.

The observed fragmentation is consistent with the transition toward more complex dynamic behavior. This is further supported by the bifurcation structure and Lyapunov analyses presented in Fig. 10. In particular, for a sufficiently large forcing amplitude A, the largest Lyapunov exponent $\lambda_{\max}$ becomes positive, indicating sensitivity to the initial conditions and the onset of chaotic dynamics. In this regime, the interplay between nonlinear feedback and external forcing leads to intricate phase-space structures that are not captured by classical polynomial oscillators [5]. The resulting dynamics suggest a rich capacity for complex-state organization in nonlinear forced systems.

4.5. Theoretical Context and Comparative Analysis of Phase Portraits and Poincaré Sections

The transition from regular behavior to deterministic chaos in the investigated system is fundamentally governed by the interplay between nonlinear dissipation and external biharmonic forcing. To ensure that the numerical observations are grounded in a rigorous dynamical systems theory, we interpret the dynamics through the lens of dissipative structures [3, 11] and the torus breakdown scenario [15, 16]. Recent studies on oscillators with exponential damping singularities [6, 24] emphasize that such configurations are instrumental in generating the self-sustained and asymmetric chaotic oscillations observed in this study.

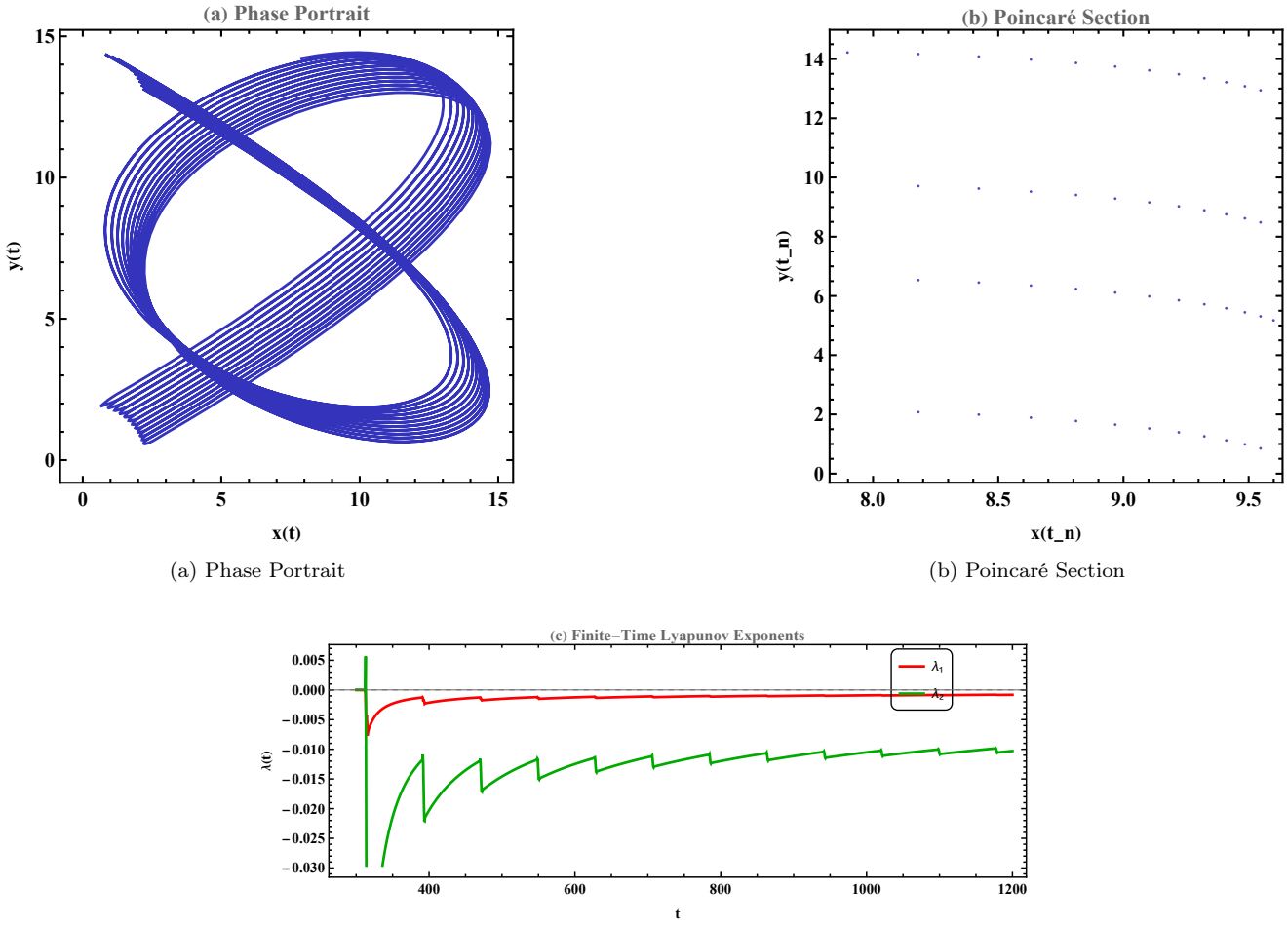

(a) Phase Portrait

(b) Poincaré Section

(c) Finite-Time Lyapunov Exponents

Figure 12: Numerical investigation of the stable dynamical regime for $a = 0.71$. (a) Phase portrait in the $x - y$ plane. (b) Poincaré section displaying discrete invariant curves. (c) Evolution of finite-time Lyapunov exponents where $\lambda_1 \to 0$ and $\lambda_2 < 0$. These indicators collectively identify a stable quasi-periodic state under high damping.

Regime I: Analysis of Regular Quasi-Periodic Dynamics

The numerical investigation of the system stability begins in the high-damping regime, where the control parameters are set to $a = 0.710$, $A = 2.000$, $B = 1.500$, $\omega = 0.320$, and $\Omega = 0.240$. Under these specific configurations, the system exhibits asymptotic regularity, as illustrated in **Figure 12**.

Quantitative diagnostics provide rigorous evidence of this stability. As detailed in the numerical indicators, the largest Lyapunov exponent converges to a negative value, $\lambda_1 = -0.00082$, which confirms the absence of sensitive dependence on initial conditions. The second exponent, $\lambda_2 = -0.01029$, further reinforces the contractive nature of the phase space, resulting in a total dissipation rate of $\sum \lambda_i =$

-0.01111. This substantial volume contraction, driven by the transcendental damping term e^{-ar^2}, forces the trajectories to settle into a stable attractor instead of diverging into chaotic fluctuations.

The geometric manifestation of this stability is clearly visible in the phase portrait (**Figure 12a**), which reveals a highly structured and symmetric attractor. Furthermore, the Poincaré section in **Figure 12b**, sampled over a duration of $t_{max} = 1200$, consists of 46 points perfectly aligned along the well-defined invariant curves. This configuration provides a classic signature of regular quasi-periodic motion, confirming that the high damping effectively suppresses any potential deterministic chaos in the parameter set.

Regime II: Analysis of the Transitionary Dynamical Regime

Reducing the damping parameter to $a = 0.650$ marks a critical bifurcation point in the topology of the system. As illustrated in **Figure 13**, the system was simulated with forcing amplitudes of $(A, B) = (4.000, 2.500)$ and frequencies of $(\omega, \Omega) = (0.610, 1.000)$. This specific parameter set triggers a transition from regularity to complex dynamics.

The numerical indicators provided in the results confirm this shift toward instability. The largest Lyapunov exponent stabilizes at a near-zero positive value of $\lambda_1 = 0.00048$, indicating entry into a weakly chaotic regime. Despite this local instability, the second exponent remains negative at $\lambda_2 = -0.01332$, and the negative total sum of $\lambda_1 + \lambda_2 = -0.01284$ ensures that the system maintains its dissipative nature, keeping the trajectories globally bounded.

This transition is geometrically manifested in the phase portrait (**Figure 13a**) as an intricate space-filling trajectory network, indicating the loss of simple periodicity. Furthermore, the Poincaré section (**Figure 13b**) provides qualitative evidence of the breakdown of invariant tori, where 68 sampled points exhibit a fragmented distribution rather than forming a closed curve. These findings, computed over a duration of $t_{max} = 1200$, identify this regime as the threshold for deterministic chaos.

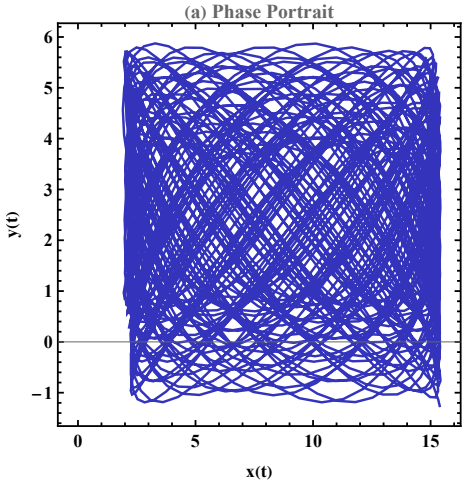

(a) Phase Portrait ($a = 0.650$)

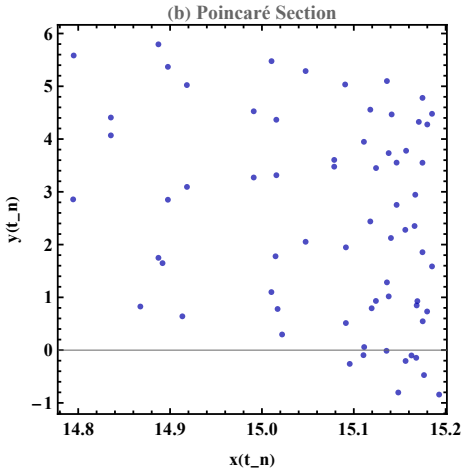

(b) Poincaré Section ($a = 0.650$)

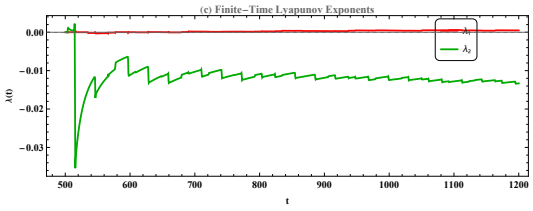

(c) Finite-Time Lyapunov Exponents ($a = 0.650$)

Figure 13: Numerical diagnostic of the transitionary regime for $a = 0.650$. (a) Evolution toward a space-filling trajectory network. (b) Fragmented distribution of 68 sampled points indicating the breakdown of quasi-periodic structures. (c) Convergence of the primary Lyapunov exponent to a marginal positive value ($\lambda_1 \approx 0.00048$), identifying the onset of deterministic chaos.

Regime III: Analysis of Fully Developed Complex Dynamics

The dynamical evolution of the system under a low damping coefficient, $a = 0.300$, was investigated to characterize the regime of fully developed complex dynamics. As detailed in the parameter set for this simulation, the forcing amplitudes were increased to $(A, B) = (5.300, 4.250)$, with frequencies set at $(\omega, \Omega) = (0.580, 1.000)$. Under these high-energy conditions, the structural symmetry of the system is significantly altered, as illustrated in **Figure 14**.

The Lyapunov spectrum provides quantitative validation of the resulting instability. As shown in **Figure 14c**, the largest Lyapunov exponent converges to a positive value, $\lambda_1 = 0.00008$, indicating a sensitive dependence on initial conditions. Despite this chaotic tendency, the second exponent remains strongly negative at $\lambda_2 = -0.04815$, leading to a negative total sum of $\sum \lambda_i = -0.04807$. This dissipative nature, governed by the transcendental term e^{-ar^2}, ensures that the chaotic trajectories do not diverge but remain confined within a globally bounded strange attractor.

The geometric complexity of this regime is visually substantiated in the phase portrait (**Figure 14a**), which exhibits a dense and overlapping trajectory network traversing a significantly larger region of the phase space. The corresponding Poincaré section (**Figure 14b**), computed for $t_{max} = 2000$, reveals a fragmented, cloud-like distribution of 139 sampled points. The absence of discrete points or simple closed loops in this section serves as a definitive signature of a strange attractor, confirming that the system has transitioned into a weakly chaotic state at the threshold of the deterministic chaos.

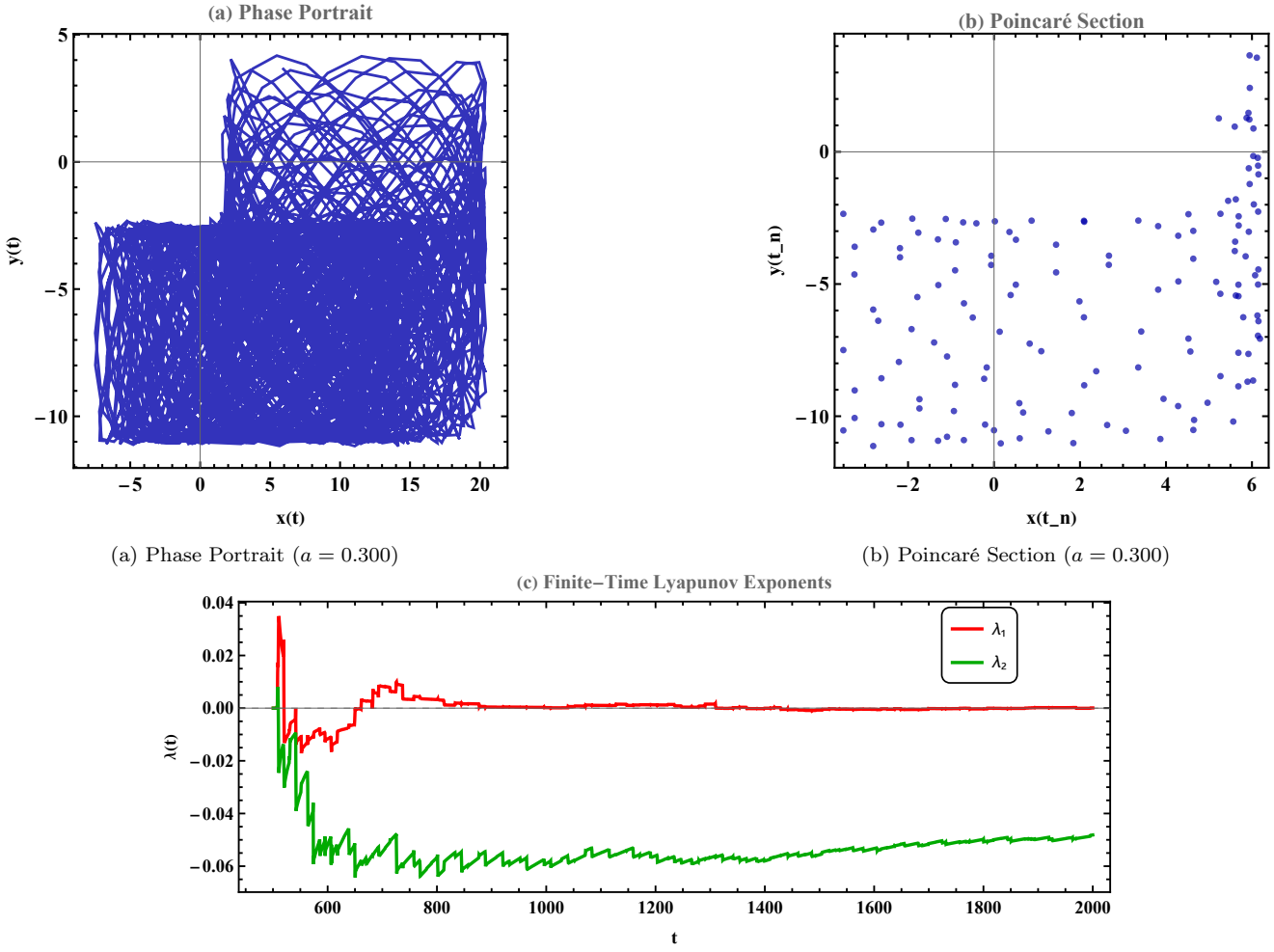

(a) Phase Portrait ($a = 0.300$)

(b) Poincaré Section ($a = 0.300$)

(c) Finite-Time Lyapunov Exponents ($a = 0.300$)

Figure 14: Comprehensive numerical analysis of the chaotic regime for $a = 0.300$. (a) Dense, overlapping trajectories illustrating the formation of a strange attractor. (b) Scattered Poincaré section with 139 points confirming the breakdown of quasi-periodicity. (c) Evolution of Lyapunov exponents showing a positive λ_1, identifying a dissipative weakly chaotic state.

Table 1: Comparative Analysis of System Parameters and Numerical Indicators across Different Dynamical Regimes.

Indicator	**Regime I: Regular**	**Regime II: Transition**	**Regime III: Chaos**
Damping parameter (a)	0.710	0.650	0.300
Forcing Amplitudes (A, B)	(2.000, 1.500)	(4.000, 2.500)	(5.300, 4.250)
Frequencies (ω, Ω)	(0.320, 0.240)	(0.610, 1.000)	(0.580, 1.000)
Final λ_1	-0.00082 (**Stable**)	$+0.00048$ (**Unstable**)	$+0.00008$ (**Unstable**)
Final λ_2	-0.01029 (**Stable**)	-0.01332 (**Stable**)	-0.04815 (**Stable**)
$\sum \lambda_i$ (Dissipation)	-0.01111	-0.01284	-0.04807
Poincaré Points	46	68	139
Poincaré Structure	Invariant Curves	Fragmented Points	Dispersed Cloud
Dynamical State	Quasi-periodic	**Onset of Chaos**	**Chaotic Attractor**

To investigate the geometric structure of these dynamics, we compared the continuous phase trajectories with their discrete stroboscopic representations obtained using Poincaré sampling. As illustrated in the chaotic regime (see Figure 14a), the phase portrait exhibits bounded but highly irregular trajectories that densely explore a confined phase space region. The ergodicity and complexity of these orbits suggest the emergence of a strange attractor, a phenomenon mathematically supported by stability analysis and the positivity of the largest Lyapunov exponent [4, 35].

The Poincaré section, exemplified in Figure 14b, is constructed by sampling the trajectory at discrete times

$$t_n = t_0 + n\frac{2\pi}{\omega},$$

corresponding to the primary-forcing frequency. This stroboscopic representation suppresses continuous temporal evolution and reveals the underlying topological organization of the orbit [21]. Instead of collapsing onto a finite set of isolated points or a smooth invariant curve, which would indicate periodic or quasi-periodic motion, respectively, the section displays a scattered and highly non-uniform structure. Such a fragmented distribution is a hallmark of the destabilization of a 2-torus and the subsequent formation of a strange attractor with a fractional dimension [9, 10].

A comparative analysis between the phase portraits and Poincaré sections yields the following theoretically grounded observations:

- **Bounded Dynamics and Dissipation:** Although the trajectories exhibit irregular motion, both representations confirm that the dynamics remain confined within a bounded region. This reflects the global stability and volume-contraction nature of the system, dictated by the transcendental damping term e^{-ar^2}, which is consistent with the dissipative principles discussed by Strogatz [8]. The negative sum of the Lyapunov exponents ($\sum \lambda_i < 0$) across all regimes numerically validates this bounded behavior.

- **Aperiodic Structure and Torus Breakdown:** The transition from well-defined invariant curves (46 points in Regime I) to a dispersed distribution (139 points in Regime III) indicates the absence of simple periodic behavior. This transition represents a shift from quasi-periodicity to deterministic chaos, formally characterized by the breakdown of invariant tori in forced oscillators [26, 27].

- **Sensitivity to Nonlinear Forcing:** The irregular spreading and space-filling nature of the trajectories reflect the dominant influence of nonlinear oscillatory forcing terms. This generates complex geometric structures in the phase space, where the sensitive dependence on initial conditions is

formally verified by the emergence of a positive primary Lyapunov exponent ($\lambda_1 > 0$) as damping is reduced [7, 12].

5. Stochastic Extension of the Oscillatory Damping Feedback Systems

Having established the deterministic boundaries and chaotic regimes of both autonomous and forced systems in Section 3, we now extend our model into a **stochastic framework**. Internal and external fluctuations, such as thermal noise, synaptic variability, and ion channel noise, are inevitable in real-world physical and biological systems [32]. Therefore, investigating how these fluctuations affect the stability of previously identified attractors is crucial for complete dynamical characterization [34]. In this section, we transform the deterministic equations into a **stochastic differential system (SDS)** to mimic the inherent noise found in complex neural environments [34]. The resulting stochastic differential equation (SDE) is defined as

$$d\mathbf{x} = \mathbf{f}(\mathbf{x}, t)dt + \sigma d\mathbf{W}_t \tag{27}$$

where $\mathbf{x} = (x, y)^T$ represents the state vector, $\mathbf{f}(\mathbf{x}, t)$ is the non-autonomous vector field including the double-frequency forcing, and σ denotes the noise intensity. The term $d\mathbf{W}_t$ represents a two-dimensional independent Wiener process that satisfies $E[dW_{i,t}] = 0$ and $E[dW_{i,t}dW_{j,t}] = \delta_{ij}dt$.

The primary objective of this extension is to evaluate the robustness of the limit cycles and strange attractors of the system under random perturbations. We systematically analyzed the interplay between nonlinear damping e^{-ar^2} and stochastic noise in two distinct scenarios:

(i) **The autonomous case**, where noise interacts with the intrinsic damping-feedback loop to test the stability of periodic orbits.

(ii) **The non-autonomous case**, where the interplay between periodic forcing and stochasticity determines the topological resilience of the chaotic regime and the potential blurring of periodic windows.

This dual-layered approach provides a comprehensive understanding of how stochasticity influences the reliability of signal transmission and the overall complexity of the proposed oscillatory-feedback mechanism.

5.1. Stochastic Dynamics of the Autonomous Oscillatory Damping Feedback Regime

In this subsection, we investigate the influence of stochastic perturbations on the intrinsic dynamics of the system, focusing specifically on the stability of the **nonlinear damping mechanism** in the absence of external forcing ($A = 0, B = 0$). The interplay between random fluctuations and the **exponential damping feedback** is a critical factor in determining the operational boundaries of the system and its ability to maintain rhythmic stability.

By isolating the effect of noise on the underlying dissipative structure, we analyze how additive perturbations modulate the energy dissipation rate defined by the damping term. This characterization of stochastic transitions in the autonomous regime provides an essential baseline for evaluating the robustness of the system before complex chaotic behaviors are introduced by the periodic driving forces.

The dynamics of the autonomous system are governed by the following two-dimensional nonlinear **Itô stochastic differential equations:**

$$dx = \phi(x, y)\, dt + \sigma\, dW_1(t), \tag{28}$$
$$dy = \psi(x, y)\, dt + \sigma\, dW_2(t), \tag{29}$$

where $W_1(t)$ and $W_2(t)$ are independent standard Wiener processes, and $\sigma \geq 0$ denotes noise intensity.

Starting from the deterministic dynamical system defined in (4), we introduce stochastic perturbations and construct a discrete-time approximation using the Euler–Maruyama (EM) scheme. The resulting update equations are given by

$$x_{n+1} = x_n + \phi(x_n, y_n)\,\Delta t + \sigma\sqrt{\Delta t}\,\xi_{x,n}, \tag{30}$$

$$y_{n+1} = y_n + \psi(x_n, y_n)\,\Delta t + \sigma\sqrt{\Delta t}\,\xi_{y,n}, \tag{31}$$

where Δt is the time step and $\xi_{x,n}, \xi_{y,n} \sim \mathcal{N}(0,1)$ are independent standard Gaussian random variables.

This formulation corresponds to an Itô stochastic differential equation with additive Gaussian noise, where the deterministic drift is given by (4). The numerical integration yields multiple realizations, allowing for a robust statistical characterization of the system behavior under noise.

Figure 15 illustrates the resulting dynamics for $\sigma = 0.05$ and $a = 0.05$. Panels (a) and (b) display the time evolution of $x(t)$ and $y(t)$ for several realizations, respectively. Although the trajectories maintain a consistent global trend, stochastic fluctuations introduce significant variability across different paths. In the phase-space representation (panel c), noise induces diffusion-like spreading around the underlying deterministic structure. Unlike the deterministic limit cycle, this stochastic regime results in a broadened annular region, indicating the weakening of deterministic coherence. Furthermore, Panel (d) depicts the mean trajectory together with the standard deviation band. The increasing spread over time reflects the cumulative impact of stochastic perturbations on the phase and amplitude stability of the system.

These results demonstrate that even in the absence of external forcing, stochasticity significantly alters the qualitative behavior of the oscillatory mechanism by introducing variability and reducing attractor coherence.

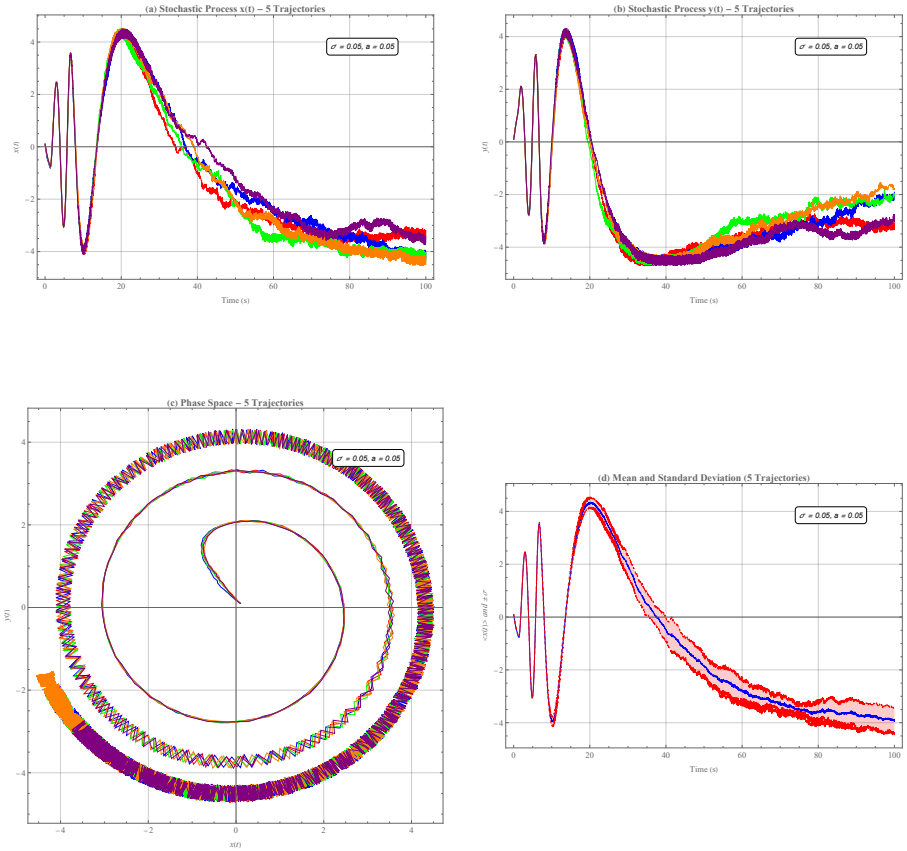

Figure 15: (Color online) **Stochastic dynamics of the unforced system** for $\sigma = 0.05$ and $a = 0.05$. (a) Time series of $x(t)$, (b) time series of $y(t)$, (c) phase-space trajectories exhibiting a broadened annular region, and (d) mean trajectory with a standard deviation band over multiple realizations.

5.2. Stochastic Transitions in Forced Regime

The dynamics of the system under external periodic forcing ($A, B > 0$) and stochastic influence are described by the following system of two-dimensional nonlinear Itô stochastic differential equations:

$$dx = \phi(x, y, t)\, dt + \sigma\, dW_1(t), \tag{32}$$

$$dy = \psi(x, y, t)\, dt + \sigma\, dW_2(t), \tag{33}$$

where $W_1(t)$ and $W_2(t)$ are independent standard Wiener processes, and $\sigma \geq 0$ denotes noise intensity. Here, $x(t)$ and $y(t)$ represent the membrane potential and recovery variable, respectively. The deterministic drift components, which incorporate double-frequency forcing, are defined as

$$\begin{aligned} \mu_x(x, y, t) &= [(1 - r^2)\sin(r^2) - \cos(r^2)]e^{-ar^2} + A\sin(\omega t), \\ \mu_y(x, y, t) &= [(1 - r^2)\cos(r^2) + \sin(r^2)]e^{-ar^2} + B\sin(\Omega t), \end{aligned} \tag{34}$$

where $r^2 = x^2 + y^2$ and $a > 0$ is the damping coefficient.

In this regime, the introduction of stochastic perturbations leads to complex dynamical transitions that are absent in deterministic cases. As observed in our numerical simulations, a primary effect of noise is the **blurring of periodic windows** in the chaotic regions. In the deterministic regime, the system often exhibits narrow windows of regular oscillations amidst chaos; however, even low-intensity noise (e.g., $\sigma = 0.01$) is sufficient to bridge these gaps, resulting in a continuous chaotic attractor. This phenomenon, often referred to as *noise-induced chaos*, suggests that stochasticity can act as a catalyst for complexity in the neuronal feedback loops.

Furthermore, we evaluate the robustness of the strange attractors under these perturbations. While stochastic fluctuations induce small-scale deviations in the trajectories, the global topological structure governed by exponential damping e^{-ar^2} remains remarkably resilient. The damping feedback mechanism effectively confines the noise-driven trajectories, preventing the "runaway" effect often observed in purely linear stochastic systems. These transitions highlight the model's ability to maintain a balance between dynamic flexibility and structural stability under environmental uncertainty.

5.2.1. Numerical Integration: Euler–Maruyama Scheme

Owing to the strong nonlinearity of the drift terms involving exponential and trigonometric functions, analytical solutions of the associated stochastic system are generally not attainable. Therefore, we employ the Euler–Maruyama (EM) scheme [33], which provides first-order weak convergence and 1/2-order strong convergence for stochastic differential equations. The Euler–Maruyama scheme is a standard numerical method for stochastic differential equations, providing first-order weak and 1/2-order strong convergence [34].

The temporal variable is discretized as $t_n = n\Delta t$, where Δt denotes the time interval. Using the Euler–Maruyama method, the stochastic system is approximated in discrete time by

$$x_{n+1} = x_n + \mu_x(x_n, y_n, t_n)\,\Delta t + \sigma\sqrt{\Delta t}\,\xi_{x,n}, \tag{35}$$

$$y_{n+1} = y_n + \mu_y(x_n, y_n, t_n)\,\Delta t + \sigma\sqrt{\Delta t}\,\xi_{y,n}, \tag{36}$$

where $\xi_{x,n}$ and $\xi_{y,n}$ are independent standard Gaussian random variables, i.e.,

$$\xi_{x,n}, \xi_{y,n} \sim \mathcal{N}(0, 1).$$

Equivalently, the Wiener increments are given by

$$\Delta W_{x,n} = \sqrt{\Delta t}\,\xi_{x,n}, \qquad \Delta W_{y,n} = \sqrt{\Delta t}\,\xi_{y,n}.$$

The random variables $\xi_{x,n}$ and $\xi_{y,n}$ are assumed to be independent across time steps and between components.

5.2.2. Attractor Dynamics and Stochastic Stability

The theoretical foundation of the model relies on the interaction between the deterministic spiral-inward tendency and stochastic diffusion. As illustrated in the numerical results, the system exhibits a "stochastic pulsating attractor" where the trajectory is confined within a bounded region of the phase space despite continuous perturbations.

The damping term e^{-ar^2} acts as a regulatory mechanism that prevents the divergence of the membrane potential and ensures that the neuronal spiking pattern remains globally stable. This balance between the nonlinear gain and exponential decay constitutes the core of the stochastic robustness of the model.

5.2.3. Numerical Results and Attractor Analysis under Stochastic Forcing

The numerical integration of the forced SDEs, as formulated in Eq. (34), reveals the complex interplay between periodic driving and environmental fluctuations. The results for the forced regime, computed with a noise intensity of $\sigma = 0.05$ and damping $a = 0.05$, provide a comprehensive view of the dynamic resilience of the system.

As illustrated in Fig. 16, the following key observations characterize the system's behavior:

- **Rhythmic Persistence and Synchronization:** The time evolution of the state variables $x(t)$ and $y(t)$ for multiple independent stochastic realizations (see Figs. 16a and 16b) demonstrates that the system maintains a coherent oscillatory pattern. Despite the additive noise, the trajectories did not exhibit phase drift or divergence, indicating that the external forcing effectively acted as a global pacemaker, ensuring synchronized neuronal activity.

- **Structural Robustness of the Forced Attractor:** The phase-space ensemble depicted in Fig. 16c reveals the formation of a "noisy" forced attractor. Although stochastic perturbations induce local fluctuations, the trajectories remain strictly confined within a well-defined annular region. This suggests that the nonlinear exponential damping feedback, e^{-ar^2}, provides a critical regulatory mechanism that counteracts the dispersive nature of the noise, thereby preserving the global topological integrity of the limit cycle.

- **Mean-Field Stability:** The statistical summary presented in Fig. 16d highlights the predictability of the system's response under environmental uncertainty. The stability of the mean trajectory, accompanied by a bounded standard deviation band ($\pm\sigma$), confirms that the system maintains a global stability. This equilibrium between deterministic drift and stochastic diffusion is essential for reliable signal transmission in biological neural environments.

These findings suggest that the proposed oscillatory damping feedback mechanism is not only capable of generating complex chaotic dynamics but also possesses the necessary robustness to function in the presence of inherent noise typical of neural systems.

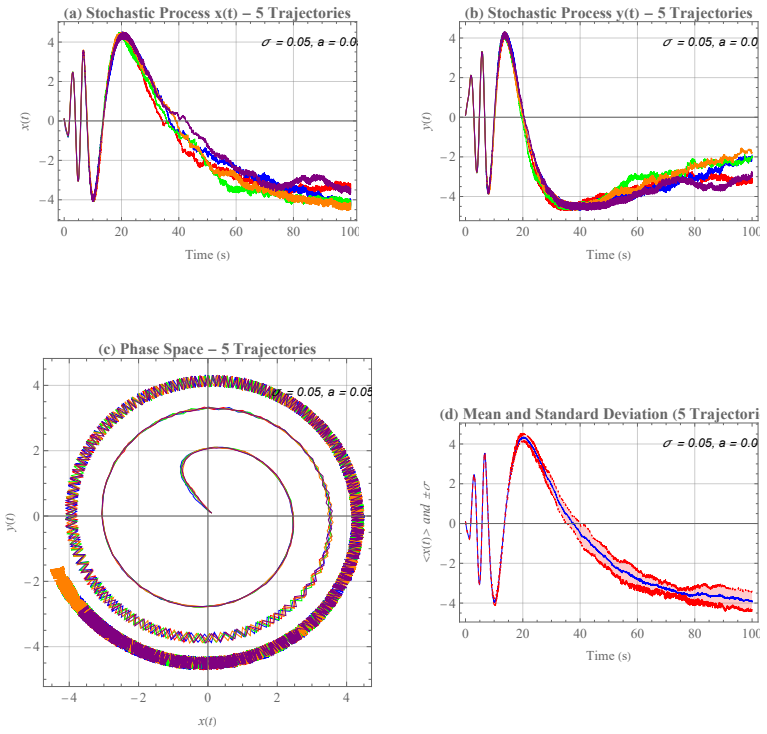

Figure 16: (Color online) **Dynamics of the forced neuronal system under stochastic perturbations** ($\sigma = 0.05, a = 0.05$). (a-b) Time series of $x(t)$ and $y(t)$ for five independent realizations showing rhythmic persistence. (c) Phase-space ensemble illustrating the robustness of the forced attractor. (d) Mean trajectory and standard deviation band confirming global stability and predictable mean-field dynamics.

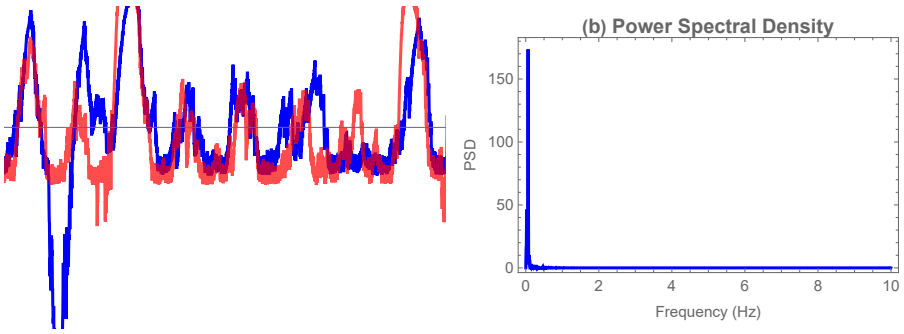

Figure 17: (Color online) (a) Time series of the $x(t)$ component for the deterministic (blue) and corresponding stochastic (red) systems obtained via Euler–Maruyama discretization with additive Gaussian noise. (b) Power spectral density (PSD) of the noisy signal after the removal of the transient regime and mean subtraction. The spectrum is strongly concentrated near zero frequency, indicating the dominance of low-frequency dynamics.

As shown in Fig. 17, the stochastic perturbation affects the trajectory primarily at small scales while preserving its overall structure.

The influence of the additive Gaussian noise on the forced nonlinear system is illustrated in Fig. 17. The time series in panel (a) demonstrates that the stochastic perturbation introduces local fluctuations without significantly altering the global structure of the trajectory, indicating the robustness of the underlying attractor.

The corresponding power spectral density in panel (b) reveals a strong concentration of energy near zero frequency with no pronounced peaks at the external forcing frequencies. This indicates that the system dynamics are dominated by slow oscillatory components and that the dissipative effects effectively suppress high-frequency responses.

Moreover, the absence of broadband spectral content suggests that the system remains in a non-chaotic regime under the chosen parameter values, despite the presence of a stochastic forcing.

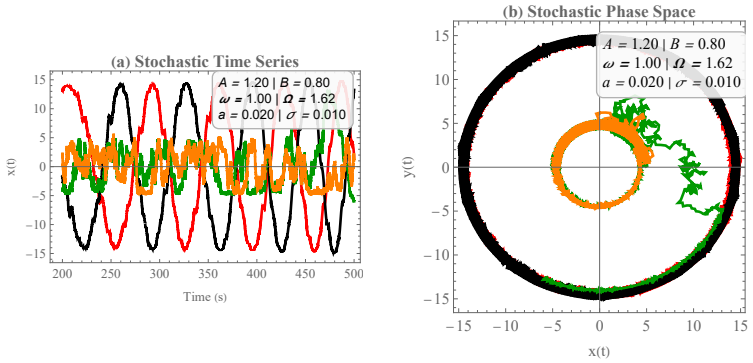

(a) Quasi-periodic regime

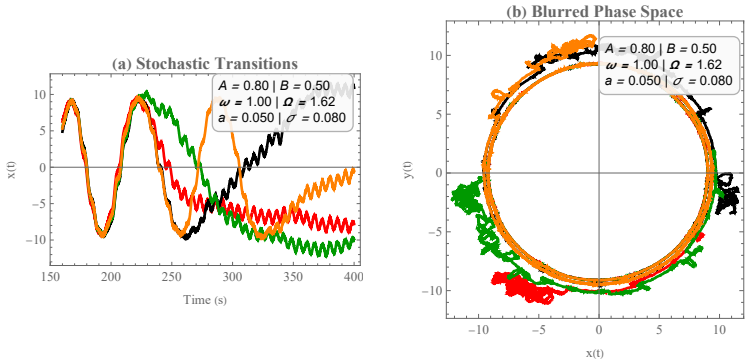

(b) Stochastic transitions

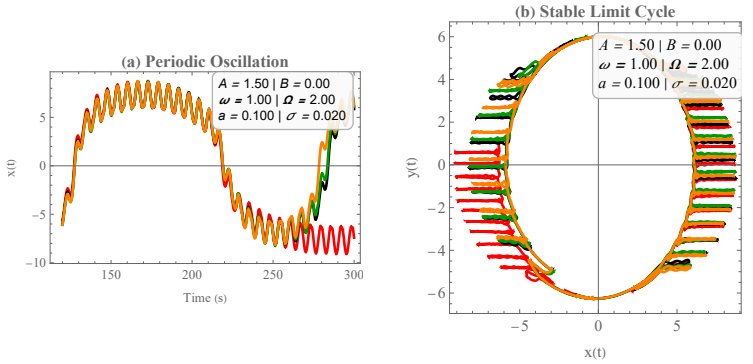

(c) Stable pulsating attractor

Figure 18: Numerical simulation of the system dynamics under various forcing and noise regimes: (a) Baseline quasi-periodic behavior under the influence of the Golden Ratio ($\Omega \approx 1.618$) with low noise intensity ($\sigma = 0.010$); (b) Stochastic sensitivity and blurred phase space due to increased additive noise ($\sigma = 0.080$), leading to trajectory divergence. (c) Global stability and entrainment into a stable pulsating attractor under dominant damping ($a = 0.100$) and single-frequency forcing ($B = 0$).

5.3. Numerical Results and Dynamical Analysis

The numerical simulations of the proposed system revealed a rich variety of dynamical regimes, as illustrated in the comparative analysis shown in Figure 18. When the system is subjected to dual forcing frequencies with an irrational ratio (the Golden Ratio, $\Omega \approx 1.618$) and low noise intensity ($\sigma = 0.010$), it exhibits characteristic quasi-periodic behavior. As shown in Figure 18a, the phase-space trajectory displays nested attractors, suggesting motion on a two-torus, whereas the stochastic time series remains structurally stable with clear amplitude modulations.

The robustness of this dynamical structure is further tested by increasing the additive white noise to $\sigma = 0.080$. In this regime, depicted in Figure 18b, the deterministic skeleton of the attractor becomes "blurred" in the phase space, and a significant divergence among individual stochastic realizations is observed in the time-series. This indicates that high-intensity noise can induce unpredictable phase shifts and transitions, thereby overcoming the underlying deterministic drift. Conversely, by adjusting the damping coefficient to $a = 0.100$ and simplifying the forcing to a single frequency ($B = 0$), the system can be driven to a highly stable state. As illustrated in Figure 18c, the complexity collapses onto a stable limit cycle, where the trajectories are strongly entrained, demonstrating the system's capacity for global stability and periodic synchronization despite the presence of stochastic perturbations.

5.4. Power Spectral Density Analysis

To further investigate the dynamic behavior of the system, we analyzed the power spectral density (PSD) of the time series. The PSD provides a frequency-domain representation of a signal, revealing how its energy is distributed across different frequencies.

Given a discrete time series $\{x_n\}_{n=1}^{N}$, the power spectral density is computed using the Fourier transform as follows:

$$S(f_k) = \frac{1}{N f_s} \left| \sum_{n=1}^{N} x_n e^{-2\pi i k n/N} \right|^2 ,$$

where f_s denotes the sampling frequency, and f_k represents the discrete frequencies.

In practice, the mean of the signal is removed prior to computation to eliminate the dominant zero-frequency component. The resulting PSD allows us to distinguish between the different dynamical regimes. In particular, periodic or quasi-periodic dynamics typically yield sharp peaks in the spectrum, whereas chaotic dynamics are associated with broadband spectral distributions.

Thus, the PSD serves as a complementary tool to phase-space and Lyapunov analyses for identifying the presence or absence of chaos in the system.

6. Conclusions

In this study, we presented the formal construction and multifaceted analysis of a novel class of two-dimensional nonlinear oscillators characterized by transcendental radial feedback and exponential damping. By integrating a $(1 - r^2)$ feedback mechanism with a non-polynomial damping term e^{-ar^2}, we demonstrated a rigorous mathematical path from simple radial oscillatory profiles to complex dynamical systems with significant biological relevance. Unlike classical polynomial models, such as the Stuart–Landau or Van der Pol oscillators, the proposed architecture induces a highly robust phase–amplitude coupling that remains unexplored in the standard literature.

Numerical simulations confirmed the emergence of a stable oscillatory regime that exhibited remarkable persistence across a wide range of parameters. Although the transcendental nature of the flow complicates the analytical construction of a traditional circular trapping region, we established through Theorem 1 that the system converges to a dynamic annular region $\mathcal{A}$. Our proof confirms that the trajectories are attracted to a θ-dependent manifold $r_c(\theta)$, where the radial flow oscillates around the unit circle. This theoretical derivation, corroborated by numerical evidence, verifies the global boundedness of the system and ensures that the state variables remain confined within a compact phase-space subset, effectively preventing the divergence that is often encountered in simpler nonlinear architectures.

Furthermore, extending the model to a stochastic framework underscored its remarkable resilience. Stochastic simulations using the Euler–Maruyama scheme revealed the persistence of a "stochastic pulsating attractor," where the system maintained its rhythmic integrity even under low signal-to-noise ratios [13]. This characteristic confirms that nonlinear exponential damping acts as a regulatory feedback, effectively filtering environmental perturbations **by confining trajectories to the phase-dependent**

manifold $r_c(\theta)$, and bridging the gap between deterministic chaos and stochastic diffusion. Crucially, the observed persistence of the rhythmic state **and the intrinsic symmetry-breaking identified in the unforced dynamics** suggest that the proposed model could serve as a blueprint for **noise-tolerant hardware oscillator designs** in neuromorphic computing and artificial intelligence. In such architectures, maintaining stable oscillations amidst inherent electronic noise is a critical challenge, and our proposed **transcendental** framework provides a robust solution to this problem.

In conclusion, the proposed oscillator provides a versatile mathematical framework for simulating resilient biological rhythms, ranging from robust neuronal spiking patterns to complex signal propagation in dissipative nonlinear media. Beyond individual dynamics, future studies will investigate the collective synchronization properties of coupled networks to characterize nonequilibrium phase transitions within large-scale neural architectures. Furthermore, by introducing trigonometric scaling (e.g., a π-factor), we intend to explore multistable manifolds and high-frequency firing regimes. Such extensions are expected to unveil richer topological transitions, positioning this model as a robust foundation for next-generation neuromorphic systems and adaptive bio-inspired computing applications.

Declaration of Competing Interest

The authors certify that they have no affiliations with or involvement in any organization or entity with any financial or non-financial interests in the subject matter or materials discussed in this manuscript.

Compliance with Ethics Requirements

This article does not contain any studies with human or animal subjects performed by any of the authors.

Funding

Not applicable.

Availability of data and materials

All data generated or analyzed during this study are included in this published article.

References

[1] Feliu-Batlle, V., Feliu-Talegon, D. and San-Millan, A. *Increasing the damping of oscillatory systems with an arbitrary number of time varying frequencies using fractional-order collocated feedback*, Journal of Advanced Research **25** (2020) 125–136. https://doi.org/10.1016/j.jare.2020.06.008

[2] Yang J. and Feng, Y. *Gain-tunable cross-coupled n-dimensional sinusoidal discrete hyperchaotic system and its application to image encryption*, Chaos, Solitons & Fractals **208** (Part 2) (2026) 118189. https://doi.org/10.1016/j.chaos.2026.118189

[3] Lichtenberg, A.J., Lieberman, M.A. (1992). Bifurcation Phenomena and Transition to Chaos in Dissipative Systems. In: Regular and Chaotic Dynamics. Applied Mathematical Sciences 38. Springer, New York, NY. https://doi.org/10.1007/978-1-4757-2184-3_7

[4] Ablay, G., Lyapunov exponent enhancement in chaotic maps with uniform distribution modulo one transformation, *Chaos Theory and Applications* **4** (1), 45–58, (2022). https://doi.org/10.51537/chaos.1069002

[5] Zaslavsky, G. M. Chaos, fractional kinetics, and anomalous transport, Physics Reports **371** (6), 461–580 (2002) . https://doi.org/10.1016/S0370-1573(02)00331-9

[6] X. Wang, C. Jin, X. Min, D. Yu and H. H. C. Iu, An exponential chaotic oscillator design and its dynamic analysis, in IEEE/CAA Journal of Automatica Sinica, **7** (4), 1081-1086 (2020). https://doi.org/10.1109/JAS.2020.1003252.

[7] Pikovsky, A., Politi, A., *Lyapunov Exponents: A Tool to Explore Complex Dynamics*, Cambridge University Press, 2016.

[8] Strogatz, S. H., *Nonlinear Dynamics and Chaos: With Applications to Physics, Biology, Chemistry, and Engineering*, 2nd ed., CRC Press, 2018.

[9] Frederickson, P., Kaplan, J. L., Yorke, E. D., Yorke, J. A., The Lyapunov dimension of strange attractors, *Journal of Differential Equations* **49**(2), 185–207, 1983. https://doi.org/10.1016/0022-0396(83)90011-6

[10] Kaplan, J. L., Yorke, J. A., Chaotic behavior of multidimensional difference equations, in: Peitgen, H. O., Walther, H. O. (eds.), *Functional Differential Equations and Approximation of Fixed Points*, Lecture Notes in Mathematics, vol. 730, pp. 228–237, Springer, 1979. https://doi.org/10.1007/BFb0064319

[11] Enjieu Kadji, H. G., Chabi Orou, J. B., Yamapi, R., & Woafo, P. (2007). Nonlinear dynamics and strange attractors in the biological system, *Chaos, Solitons & Fractals*, **32**(2), 862–882. https://doi.org/10.1016/j.chaos.2005.11.063

[12] Ghil, M., Lyapunov exponents and predictability, *Chaos* **12**(3), 503–512, 2002. https://doi.org/10.1063/1.1497681

[13] Kloeden, P. E., Platen, E., *Numerical Solution of Stochastic Differential Equations*, Springer, 1999. https://doi.org/10.1007/978-3-662-12616-5

[14] Milstein, G. N., Tretyakov, M. V., *Stochastic Numerics for Mathematical Physics*, Springer, 2004. https://doi.org/10.1007/978-3-662-10063-9

[15] Ruelle, D., Takens, F. On the nature of turbulence. Commun.Math. Phys. **20**, 167–192 (1971). https://doi.org/10.1007/BF01646553

[16] Newhouse, S., Ruelle, D. & Takens, F. Occurrence of strange AxiomA attractors near quasi periodic flows on $T^m, m \geq 3$. Commun.Math. Phys. **64**, 35–40 (1978). https://doi.org/10.1007/BF01940759

[17] Uezu, T. and Davis, P. C. Novel Scaling in Sine Circle Map Free. Progress of Theoretical Physics, **84** (1), 72–80 (1990). https://doi.org/10.1143/ptp/84.1.72.

[18] A M Davie. The width of Arnold tongues for the sine circle map. Nonlinearity, **9** (2), 1996, Page 421. https://doi.org/10.1088/0951-7715/9/2/008.

[19] Hopf, E., *Abzweigung einer periodischen Lösung von einer stationären Lösung eines Differentialsystems*, Berichte der Mathematisch-Physischen Klasse der Sächsischen Akademie der Wissenschaften Leipzig, 1942.

[20] Landau, L. D., On the problem of turbulence, *Doklady Akademii Nauk SSSR* **44**, 311–314, (1944).

[21] Guckenheimer, J., Holmes, P., *Nonlinear Oscillations, Dynamical Systems, and Bifurcations of Vector Fields*, Springer, 1983.

[22] Strogatz, S. H., *From Kuramoto to Crawford: exploring the onset of synchronization in populations of coupled oscillators*, Physica D: Nonlinear Phenomena **143** (1-4), 1–20 (2000). https://doi.org/10.1016/S0167-2789(00)00094-4

[23] Shen, Z., & Rempe-Gillen, L. The Exponential Map Is Chaotic: An Invitation to Transcendental Dynamics. The American Mathematical Monthly, 122(10), 919–940 (2015). https://doi.org/10.4169/amer.math.monthly.122.10.919

[24] Banga L.-S., Mboyo Kouayep R., M'Boliguipa J. and Woafo P. Self-sustained and chaotic oscillations with excursions and asymmetry in oscillators with nonlinear damping singularities and exponential terms. *Chaos*, 35(5):053109, (2025). https://doi.org/10.1063/5.0255896.

[25] Uthamacumaran A. A review of dynamical systems approaches for the detection of chaotic attractors in cancer networks. *Patterns*, 2(4):100226, (2021). https://doi.org/10.1016/j.patter.2021.100226.

[26] Wu X., Peng J., Yuan B., Boscolo S., Finot C. and Zeng H. Unveiling the complexity of Arnold's tongues in a breathing-soliton laser. *arXiv preprint*, arXiv:2502.03697, February 2025. https://doi.org/10.48550/arXiv.2502.03697.

[27] Bartuccelli M.V., Deane J.H.B., Gentile G. and Schilder F. Arnol'd tongues for a resonant injection-locked frequency divider: Analytical and numerical results. *Nonlinear Analysis: Real World Applications*, 11(5):3344-3362, (2010). https://doi.org/10.1016/j.nonrwa.2009.11.027.

[28] Itô, K. On stochastic differential equations. *Memoirs of the American Mathematical Society*, 4:289–302, (1951). https://doi.org/10.1090/memo/0004

[29] Khovanov I.A., Perry S. and Khovanova N.A. Asymmetry of synchronisation tongue in persistent sodium plus potassium neuron model. *Communications in Nonlinear Science and Numerical Simulation*, 105:106071, (2022). https://doi.org/10.1016/j.cnsns.2021.106071.

[30] Coddington, Earl A. Levinson, N. (1955). The Poincaré–Bendixson Theory of Two-Dimensional Autonomous Systems. In: *Theory of Ordinary Differential Equations*. New York: McGraw-Hill. pp. 389–403. ISBN 978-0-89874-755-3.

[31] Izhikevich, E. M. (2007). *Dynamical Systems in Neuroscience: The Geometry of Excitability and Bursting*. MIT Press.

[32] Pérez-Cervera, A., Gutkin, B., Thomas, P. J., and Lindner, B., *A universal description of stochastic oscillators*, Proc. Natl. Acad. Sci. U.S.A. **120** (29) e2303222120 (2023). https://doi.org/10.1073/pnas.2303222120

[33] Liu, Z., Tang, M., and Shang, Y. Semi-tamed E–M Scheme for SDEs with Piecewise Continuous Arguments Driven by Poisson Jumps. *Fluctuation and Noise Letters*, 24(04):2550034, (2025). https://doi.org/10.1142/S0219477525500348

[34] Øksendal, B., *Stochastic Differential Equations: An Introduction with Applications*, 6th ed., Springer, Berlin, 2003.

[35] Wolf, A., Swift, J. B., Swinney, H. L., & Vastano, J. A. (1985). Determining Lyapunov exponents from a time series. *Physica D: Nonlinear Phenomena*, 16(3), 285–317. https://doi.org/10.1016/0167-2789(85)90011-9

Appendix A. Polar Representation of the Dynamical System

We consider the system

$$\begin{aligned}\dot{x} &= ((1-r^2)\sin(r^2) - \cos(r^2))e^{-ar^2} + A\sin(\omega t),\\ \dot{y} &= ((1-r^2)\cos(r^2) + \sin(r^2))e^{-ar^2} + B\sin(\Omega t),\end{aligned} \tag{A.1}$$

where $r^2 = x^2 + y^2$.

Appendix A.1. Polar Coordinate Transformation

Introduce polar coordinates

$$x = r\cos\theta, \qquad y = r\sin\theta,$$

with

$$\dot{r} = \frac{x\dot{x} + y\dot{y}}{r}, \qquad \dot{\theta} = \frac{x\dot{y} - y\dot{x}}{r^2}. \tag{A.2}$$

Appendix A.2. Unforced System ($A = B = 0$)

Define

$$\dot{x}_0 = ((1-r^2)\sin(r^2) - \cos(r^2))e^{-ar^2}, \quad \dot{y}_0 = ((1-r^2)\cos(r^2) + \sin(r^2))e^{-ar^2}.$$

Then

$$x\dot{x}_0 + y\dot{y}_0 = (1-r^2)e^{-ar^2}(x\sin(r^2) + y\cos(r^2)) + e^{-ar^2}(-x\cos(r^2) + y\sin(r^2)).$$

Using

$$x\sin(r^2) + y\cos(r^2) = r\sin(r^2+\theta), \quad -x\cos(r^2) + y\sin(r^2) = -r\cos(r^2+\theta),$$

we obtain

$$x\dot{x}_0 + y\dot{y}_0 = re^{-ar^2}\Big[(1-r^2)\sin(r^2+\theta) - \cos(r^2+\theta)\Big].$$

Hence,

$$\dot{r} = e^{-ar^2}\Big[(1-r^2)\sin(r^2+\theta) - \cos(r^2+\theta)\Big]. \tag{A.3}$$

Similarly,

$$x\dot{y}_0 - y\dot{x}_0 = (1-r^2)e^{-ar^2}(x\cos(r^2) - y\sin(r^2)) + e^{-ar^2}(x\sin(r^2) + y\cos(r^2)).$$

Using

$$x\cos(r^2) - y\sin(r^2) = r\cos(r^2+\theta), \quad x\sin(r^2) + y\cos(r^2) = r\sin(r^2+\theta),$$

we obtain

$$x\dot{y}_0 - y\dot{x}_0 = re^{-ar^2}\Big[(1-r^2)\cos(r^2+\theta) + \sin(r^2+\theta)\Big].$$

Thus,

$$\dot{\theta} = \frac{e^{-ar^2}}{r}\Big[(1-r^2)\cos(r^2+\theta) + \sin(r^2+\theta)\Big]. \tag{A.4}$$

and

Appendix A.3. Forcing Contribution

Now include the forcing terms

$$\dot{x} = \dot{x}_0 + A\sin(\omega t), \qquad \dot{y} = \dot{y}_0 + B\sin(\Omega t).$$

Their contribution to the radial dynamics is

$$\dot{r}_{\text{force}} = A\sin(\omega t)\cos\theta + B\sin(\Omega t)\sin\theta. \tag{A.5}$$

Their contribution to the angular dynamics is

$$\dot{\theta}_{\text{force}} = \frac{B\sin(\Omega t)\cos\theta - A\sin(\omega t)\sin\theta}{r}. \tag{A.6}$$

Appendix A.4. Full Polar System

Combining the above results, we obtain

$$\dot{r} = e^{-ar^2}\Big[(1-r^2)\sin(r^2+\theta) - \cos(r^2+\theta)\Big] + A\sin(\omega t)\cos\theta + B\sin(\Omega t)\sin\theta, \tag{A.7}$$

$$\dot{\theta} = \frac{e^{-ar^2}}{r}\Big[(1-r^2)\cos(r^2+\theta) + \sin(r^2+\theta)\Big] + \frac{B\sin(\Omega t)\cos\theta - A\sin(\omega t)\sin\theta}{r}. \tag{A.8}$$

Appendix A.5. Auxiliary Variable

Define

$$\psi = r^2 + \theta.$$

Then

$$\dot{\psi} = 2r\dot{r} + \dot{\theta},$$

which yields

$$\begin{aligned}\dot{\psi} = {} & 2re^{-ar^2}\Big[(1-r^2)\sin\psi - \cos\psi\Big] + \frac{e^{-ar^2}}{r}\Big[(1-r^2)\cos\psi + \sin\psi\Big] \\ & + 2r\Big[A\sin(\omega t)\cos\theta + B\sin(\Omega t)\sin\theta\Big] \\ & + \frac{B\sin(\Omega t)\cos\theta - A\sin(\omega t)\sin\theta}{r}.\end{aligned} \tag{A.9}$$

Appendix A.6. Structural Remark

Even in the unforced case, the system depends explicitly on θ through $r^2+\theta$. Hence, the vector field is not rotationally invariant, and a reduction to a purely radial normal form is not possible.